Residual stress determination of ductile cast iron by means of neutron diffraction

FJ Smith

orcid.org 0000-0003-3869-8857

Dissertation submitted in partial fulfilment of the requirements for the degree *Master of Engineering in Mechanical Engineering* at the North-West University

Supervisor: Prof J Markgraaff

Co-Supervisor: Dr D Marais

Graduation May 2018

Student number: 23422114

DECLARATION

I, **Francois Smith**, declare that this dissertation is a presentation of my own original work.

Whenever contributions of others are involved, every effort was made to indicate this clearly, with due reference to the literature.

No part of this work has been submitted in the past, or is being submitted, for a degree or examination at any other university or course.

Signed on this, 19th day of November 2017, at Potchefstroom.

_____FJ Smith_____

INITIALS AND SURNAME

ACKNOWLEDGEMENTS

I would like to thank the following organisations and persons for their contributions to this research:

- The South African Nuclear Energy Corporation (Necsa) SOC Limited
- Prof J Markgraaff (North-West University)
- Dr D Marais (Necsa)
- Prof AM Venter (Necsa)
- Carien Rothman
- My parents
- Mr A McFarlane (Ametex)
- Mr E Zimmerman (Ametex)
- The Technology and Human Resources for Industry Program (THRIP)
- Mr S Naude (North-West University)
- Mr B Van der Merwe (North-West University)
- Mr T Diobe (North-West University)
- High Duty Castings (Pty) Ltd
- My Creator and Saviour

ABSTRACT

A study was undertaken to simulate the casting process, using simulation software, of a ductile iron casting (for use as a valve body) and in doing so, to determine the order of residual stress and experimentally verify the simulation results.

The simulation was carried out using MAGMASOFT® simulation software, where after the residual stress results were extracted. The residual stress results were verified using neutron diffraction strain measurements. The simulation and verification were also done on samples subjected to heat treatment and machining in order to determine the effects it had on residual stress within the components.

The measured residual stress results were found not to compare very well with the simulation predictions of MAGMASOFT®. Numerous reasons were provided for this in the report.

The residual stress results, by means of neutron diffraction versus the residual stress results obtained by the MAGMASOFT® simulation for the heat treated and machined samples, also did not compare very well. However, the results of both neutron diffraction and MAGMASOFT®, showed a decrease in residual stress.

Keywords:

Valves, Ductile Cast Iron, Residual Stress, Neutron Diffraction, MAGMASOFT®

TABLE OF CONTENTS

LIST OF FIGURES

LIST OF TABLES

LIST OF EQUATIONS

1. INTRODUCTION

1.1 Background

Piping systems which convey different types of liquids, slurries and gasses make use of valves, which are mechanical of nature, in order to control the flow and pressure of the contents (Solken, 2008). There are many different types of valves that each have different designs, practical capabilities and features. A few different types of valves that are obtainable, which are mainly classified according to their closure mechanisms, are gate -, ball -, butterfly -, diaphragm -, and globe valves, among others (Solken, 2008).

Valves can be operated manually, pneumatically or hydraulically and they have the following typical functions (Solken, 2008):

- Starting and stopping flow;
- Flow direction control;
- Increasing or decreasing flow;
- Flow or process pressure regulation; and
- Pressure relief.

All the different types of valves have different components, although most of them consist out of a valve body and a stem. The common materials from which these components are usually manufactured, are the following (KITZ Corporation, 2008):

- bronze,
- brass,
- grey cast iron,
- ductile cast iron,
- carbon steel,
- stainless steel,
- nodular graphite cast iron, and
- aluminium alloy.

The major valve suppliers/manufacturers in South Africa currently compete with countries such as China. The problem with this is not the quality of the valves as such, but rather the price thereof. This was identified because of complaints, especially regarding valves produced from ductile iron by South African industries that include high volume users such as Eskom, municipalities and Sasol (Merchantec Research, 2014).

To be able to compete with the foreign valve market, the valve suppliers/manufacturers in South Africa will need to be able to produce the valves cheaper without neglecting the quality thereof. The only way this will be possible is if, for example, the ductile iron castings (most common material that valves are made from) are optimised in terms of manufacturability time (effectiveness of the moulds used for casting), reliability improvements and weight reduction; thereby reducing costs (McFarlane, 2016).

One possible method of optimising the casting of components can be achieved by means of modern simulation software. This software is said to simulate the casting process accurately in an effort to reduce unwanted defects, for example cold shuts, blisters, misruns and residual stress. Residual stress directly influences the design and manufacturing criteria of mechanical components and can cause premature failure (Makino, 1994:1). Through optimisation, by use of software, residual stresses could be averted by changing the positions of the risers and vents.

Computational fluid dynamic programmes such as ANSYS Fluent and Star CCM+ can be used for the simulation of the mentioned casting process optimisation. According to Abou Msallem *et al*. (2010:114), FEMLAB 3.1i can be used to predict the process-induced residual stress. Another method according to Yaghi *et al*. (2006:865) as well as Bonnaud and Gunnars (2015:533), is finite element analysis software called ABAQUS. A software package called MAGMASOFT® with the module MAGMAstress, said to be a detailed multi-physics modelling software that integrates thermomechanical and phase transformation phenomenon, aims to simulate all aspects during and after the casting process and also predicts the presence of residual stress (MAGMA, 2012c).

Residual stress is almost certain to be built-up by reducing the thickness of the castings to save weight, especially in ductile iron valve bodies. Due to the residual stress being such an important factor in castings, the simulation thereof will have major advantages to avert premature failure. Therefore, it is very important for the simulation to be accurate and trustworthy.

1.2 Problem Statement

The South African casting industry, as affirmed by the South African agents of MAGMASOFT® (Ametex (Pty) Ltd.), expressed the need to independently verify the residual stresses in ductile iron valve bodies, calculated by the cast process simulation software, MAGMASOFT®.

1.3 Aim

1. To review experimental methods to verify residual stresses in castings obtained by simulation software.
2. To simulate the casting process using ductile iron (for use as a valve body), by means of MAGMASOFT® to predict and calculate the residual stresses which can be verified using a selected experimental method obtained by the review process.
3. To determine the feasibility of the method selected.

2. LITERATURE STUDY

2.1 The Casting Process

Casting has an advantage above other manufacturing processes due to its design flexibility, simplicity, cost and material selection, and performance (Warda, 1990:2-1).

The casting process is defined as follows and involves three steps (Kalpakjian & Schmid, 2014:237):

1. pouring molten metal into a mould;
2. allowing it to solidify; and
3. removing the part from the mould.

Important factors to take into consideration during casting operations is the flow of the molten metal into the mould cavity; the cooling and solidification of the molten metal in the mould; and the influence the type of material of the mould has on the casting. The casting process can be completed using different types of moulds as listed below (Kalpakjian & Schmid, 2014:257):

- Expendable moulds (see Figure 1) – which is broken up after the mould process and normally made from sand, plaster or ceramic;
- Permanent moulds – used repeatedly and normally made from metals; and
- Composite moulds – made from two or more types of materials such as metal, sand and graphite.

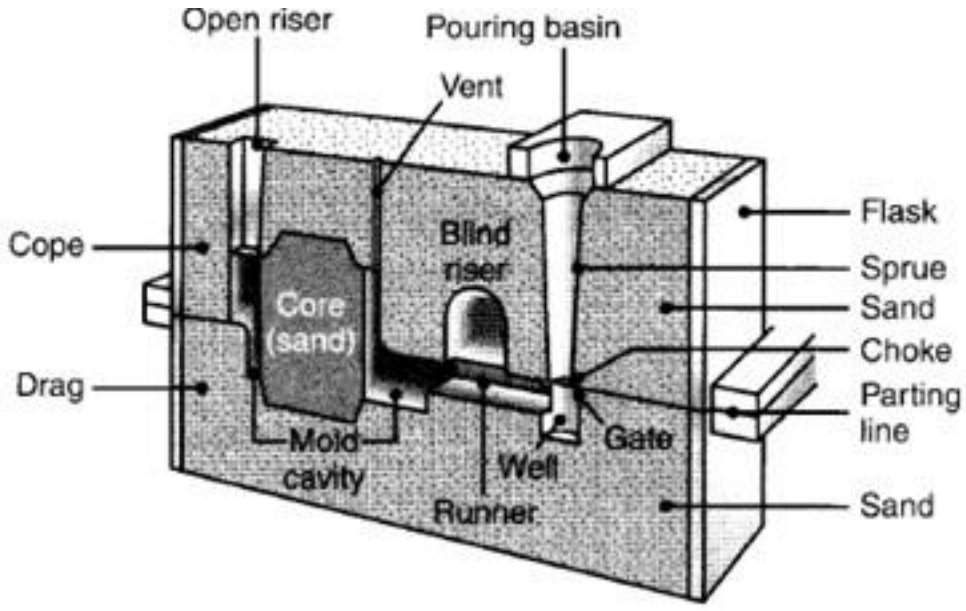

Figure 1: Typical schematic illustration of a sand mould, showing the major features in sand casting (adapted from Kalpakjian & Schmid, 2014:261)

The following types of casting alloys can be used in the process (Kalpakjian & Schmid, 2014:280; Warda, 1990:2-3):

- Cast iron,
- Aluminium,
- Zinc,
- Lead,
- Copper,
- Magnesium.

The term “Cast iron” refers to a series of materials with the main component iron and very imperative amounts of silicon (between 0.5 - 3%) and carbon (between 1.7 – 4.3%) (see Figure 2). The properties of cast irons are determined by their microstructures with the important microstructural components namely graphite, carbide, ferrite, pearlite, martensite and austenite (Warda, 1990:2-3).

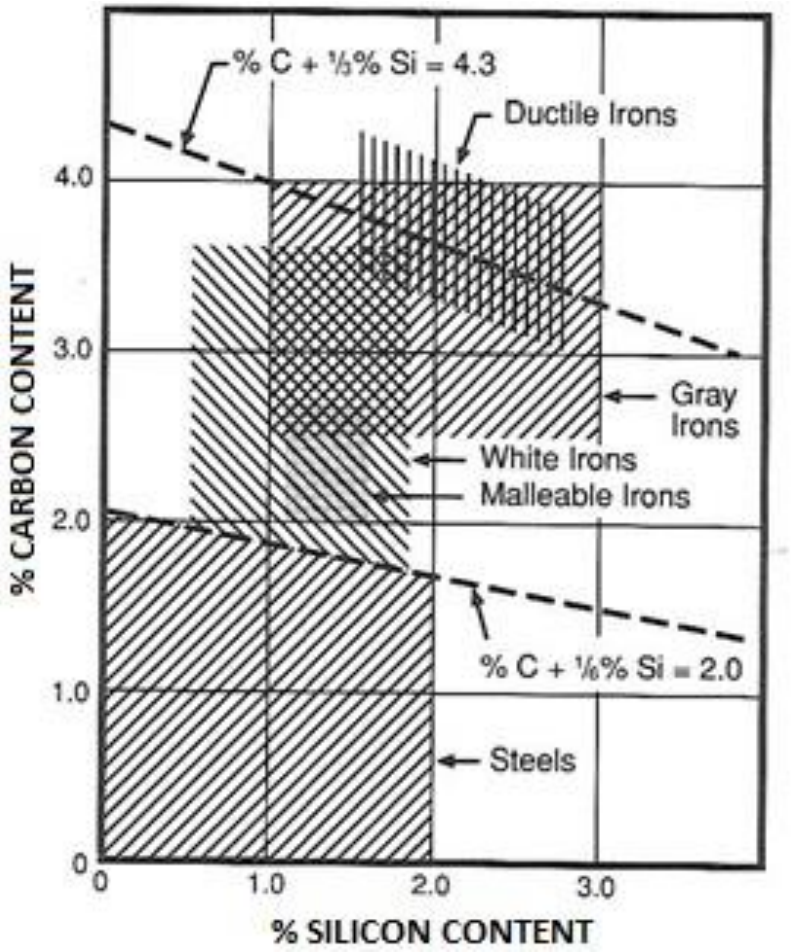

Figure 2: Approximate ranges of carbon and silicon for steel and various cast irons (adapted from Warda, 1990:2)

The most common types of cast iron are white iron, grey iron, malleable iron and ductile iron (Kalpakjian & Schmid, 2014:305; Warda, 1990:2-7). The properties and the most common applications of the above-mentioned cast irons are presented in Table 1.

Table 1: Properties and most common applications of cast irons, (adapted from Kalpakjian & Schmid, 2014:305)

Cast Iron	Type	Ultimate Tensile Strength (MPa)	Yield Strength (MPa)	% Elongation in 50 mm	Common Applications
Grey	Ferritic	170	140	0.4	Sanitary ware, Pipes
	Pearlitic	275	240	0.4	Machine tools, Engine blocks
	Martensitic	550	550	0	Wear surfaces
Ductile	Ferritic	415	275	18	Pipes, general service
	Pearlitic	550	380	6	Crankshafts, highly stressed parts
	Martensitic (Tempered)	825	620	2	High-strength machine parts, wear resistant parts
Malleable	Ferritic	365	240	18	Pipe fittings, Hardware
	Pearlitic	450	310	10	Couplings, Railroad equipment
	Martensitic (Tempered)	700	550	2	Gears, Con-rods, Railroad equipment
White	Pearlitic	275	275	0	Mill rolls, Wear-resistant parts

Ductile iron is most commonly used in the production of valve bodies in South Africa (mentioned in section 1.1) and, therefore, the next section will discuss ductile iron in more detail.

2.2 Ductile Iron

Ductile iron is widely used in automobile parts and piping systems due to it being easy to cast and having excellent mechanical properties. These properties allow ductile iron castings to obtain extremely complex geometries without any joining or welding applications (Borsato *et al*., 2017:902; Xiao *et al*., 2014:1050). The advantages that ductile iron has above the other cast irons are: a higher performance and versatility of mechanical properties at a lower cost (Warda, 1990:2-11).

There are numerous types of ductile iron based on different microstructures of the graphite that is present in the ductile iron. These differences in the ductile iron are obtained during casting by the addition of cerium or magnesium to the melt (see Figure 3). The different types of ductile iron are as follows (Warda, 1990:2-13):

- Ferritic,
- Ferritic-Pearlitic,
- Pearlitic,
- Martensitic,
- Austenitic,
- Austempered.

MATRIX						
Ferritic Grade 5	Ferritic-pearlitic Grade 3	Pearlitic Grade 1	Martensitic (With retained austenite)	Tempered Martensitic	ADI Grade 230	Austenitic
415 MPa	550 MPa	690 MPa	600 MPa	790 MPa	1600 MPa	310 MPa
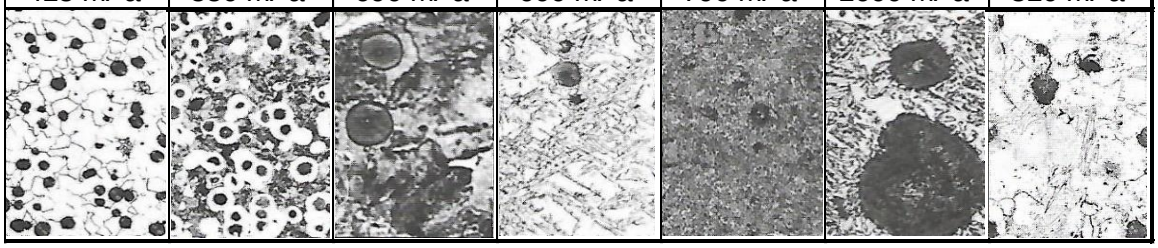						

Figure 3: Tensile strengths and microstructures for different Ductile Iron types, (adapted from Warda, 1990:2-10)

In Figure 3, it is observed that the graphite in ductile iron is in the form of spheroids and not in the form of flakes, as in the case of other cast irons. This spherical form of graphite is due to the specific amount of magnesium added to the molten metal, which then reacts with the oxygen and sulphur. Ductile iron shows a linear stress-strain relation, a substantial variety of yield strengths and high ductility (AtlasFoundry-Inc., 2016).

During the casting of ductile iron (and all other casting operations), the material needs to be cooled down from high temperatures to transform from a liquid (molten form) to a solid. The transformation process (hot to cold) entails the uneven shrinking of the material. This uneven shrinking leads to numerous problems. One of these problems, although not noticeable at first, which can lead to failures in castings, is called residual stress.

2.3 Stress and Residual Stress

Before residual stress can be discussed, we need to understand the mechanism behind stress itself. The notion of stress is when external forces act on a body or when one body exerts a force on its neighbouring body. The body is then said to be in a stress state. When the stress is below the elastic limit, the strain is recoverable, thus the body returns to its original shape when the stress is removed. Hooke's Law states that the amount of strain is proportionate to the magnitude of the stress applied. Furthermore, it is important to note that this is for adequately small stresses (Nye, 1985:131).

Hooke's Law states the following:

$$\varepsilon = s\sigma$$

Equation 1: Hooke's Law

where:

- ε is the longitudinal strain;
- σ is the tensile stress; and
- s is the elastic compliance constant.

For stress and strain arrangement directions, Hooke's Law determines (Nye, 1985:131):

$$\sigma = \varepsilon c$$

Equation 2: Hooke's Law rewritten

where:

- $c = \frac{1}{s}$
- c is the elastic stiffness coefficient (Young's Modulus).

Nye (1985:131), found that when a universal homogeneous stress, σ_{ij}, is applied to a crystal, the consequential homogeneous strain, ε_{ij}, is such that every component is linearly associated to all the stress components. According to Nye (1985:132), the general form of Hooke's Law is written as follows:

$$\varepsilon_{ij} = s_{ijkl}\sigma_{kl}$$

Equation 3: Hooke's Law's general form

where:

- s_{ijkl} are the crystal compliances with independent coefficients.

Equation 3 stances for nine similar equations with nine different terms on the right-hand side, thus adding up to 81 coefficients of s_{ijkl} :

$$\begin{aligned}\varepsilon_{11} = \; & s_{1111}\sigma_{11} + s_{1112}\sigma_{12} + s_{1113}\sigma_{13} + \\ & + s_{1121}\sigma_{21} + s_{1122}\sigma_{22} + s_{1123}\sigma_{23} + \\ & + s_{1131}\sigma_{31} + s_{1132}\sigma_{32} + s_{1133}\sigma_{33}\end{aligned}$$

Equation 4

If only one stress component is applied, for example σ_{11}, it is implied by Equation 4 that all the strain components can be different from 0 and not only ε_{11}. This can be explained by a rectangular crystal block with a uniaxial applied tension on its one set of edges, which will cause stretch and shear influencing more than one component.

An alternative equation to Equation 4, expressed in terms of strain, is as follows (Nye, 1985:132):

$$\sigma_{ij} = c_{ijkl}\varepsilon_{kl}$$

Equation 5

where:

- c_{ijkl} are the 81 stiffness constants of the crystal.

Nye (1985:132), states that σ_{ij} can always be seen as symmetrical, even when body-torques are present. Thus, when for example a shear stress is applied about the Ox_3 axis, the following equation will arise:

$$\varepsilon_{11} = s_{1112}\sigma_{12} + s_{1121}\sigma_{21} = (s_{1112} + s_{1121})\sigma_{12}$$

Equation 6

where:

- s_{1112} and s_{1121} always occur together; and
- Ox_3 is shown in Figure 4.

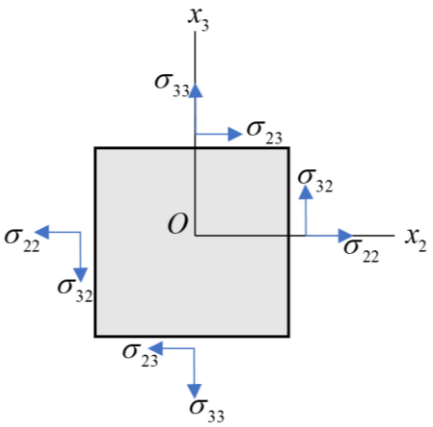

Figure 4: Axis illustration – on a unit cube in a homogenously stressed body where the forces on the faces are perpendicular to Ox_2 and Ox_3, Ox_1 is normal to the plane of the figure (adapted from Nye, 1985:84)

s_{1112} and s_{1121} always occur together and, therefore, it can be indicated that $s_{ijkl} = s_{ijkl}$ - thus, reducing the 81 stiffness constants to 36 (Nye, 1985:133).

According to Nye (1985:134), the first and last two of the s_{ijkl} and c_{ijkl} suffixes can be abbreviated into single suffixes ranging from 1 to 6 as described in the following matrix:

$$\begin{bmatrix} \sigma_{11} & \sigma_{12} & \sigma_{13} \\ \sigma_{21} & \sigma_{22} & \sigma_{23} \\ \sigma_{31} & \sigma_{32} & \sigma_{33} \end{bmatrix} \rightarrow \begin{bmatrix} \sigma_1 & \sigma_6 & \sigma_5 \\ \sigma_6 & \sigma_2 & \sigma_4 \\ \sigma_5 & \sigma_4 & \sigma_3 \end{bmatrix}$$

Equation 7

Thus, it can be summarised as follows:

Tensor notation	11	22	33	23,32	31,13	12,21
Matrix notation	1	2	3	4	5	6

Equation 3 and Equation 5 can now be presented as follows:

$$\varepsilon_i = s_{ij}\sigma_j$$

Equation 8

$$\sigma_i = c_{ij}\varepsilon_j$$

Equation 9

where:

- $(i, j = 1,2,...,6)$; and
- (s_{ij}) and (c_{ij}) are each 6 x 6 matrices.

When there is a minor change of strain in a crystal, the work done per unit volume is as follows:

$$dW = \sigma_i d\varepsilon_i$$

Equation 10

where:

- dW is the change in work done;
- $d\varepsilon$ is the change in strain; and
- $(i = 1,2,...,6)$.

Furthermore, according to Nye (1985:136-137), when the deformation process is reversible and isothermal, it equals the free energy increase, per unit volume, as follows:

$$d\psi = dW = \sigma_i d\varepsilon_i$$

Equation 11

where:

- $d\psi$ is the increase in free energy.

This results in the following, by incorporating Equation 9:

$$d\psi = c_{ij}\varepsilon_j d\varepsilon_i$$

Equation 12

Equation 12 can be presented as:

$$\frac{d\psi}{d\varepsilon_i} = c_{ij}\varepsilon_j$$

Equation 13

And by differentiating both sides with respect to ε_j:

$$\frac{d}{d\varepsilon_j}\left(\frac{d\psi}{d\varepsilon_i}\right) = c_{ij}$$

Equation 14

From this, it can be determined that $c_{ij} = c_{ji}$ and $s_{ij} = s_{ji}$ as a result of the following:

- The order of differentiation is irrelevant due to ψ being a function of only the state of the body, specified by the strain components; and

- The left side of Equation 14 is symmetrical with respect to i and j.

Due to the symmetry of the $\left(s_{ij}\right)$ and $\left(c_{ij}\right)$ matrices, the independent stiffness constants are further reduced from 36 to 21.

According to Nye (1985:137), in order to transform the $\left(s_{ij}\right)$ matrix into another coordinate system, tensor notation must be considered again. Furthermore, the elastic properties of all materials are centrosymmetric and can be fully described in terms of the symmetric axes present (Nye, 1985:137-141). Symmetrical considerations further reduce the independent stiffness constants to 6 as shown in the following matrix:

$$\begin{bmatrix} s_{11} & s_{12} & s_{13} & s_{14} & 0 & 0 \\ s_{12} & s_{11} & s_{13} & -s_{14} & 0 & 0 \\ s_{13} & s_{13} & s_{33} & 0 & 0 & 0 \\ s_{14} & -s_{14} & 0 & s_{44} & 0 & 0 \\ 0 & 0 & 0 & 0 & s_{44} & 2s_{14} \\ 0 & 0 & 0 & 0 & 2s_{14} & 2(s_{11}-s_{12}) \end{bmatrix}$$

Equation 15

To illustrate the importance of stress and strain, the relations between thermal, electrical and mechanical properties are shown in a diagram known as Heckmann's Diagram.

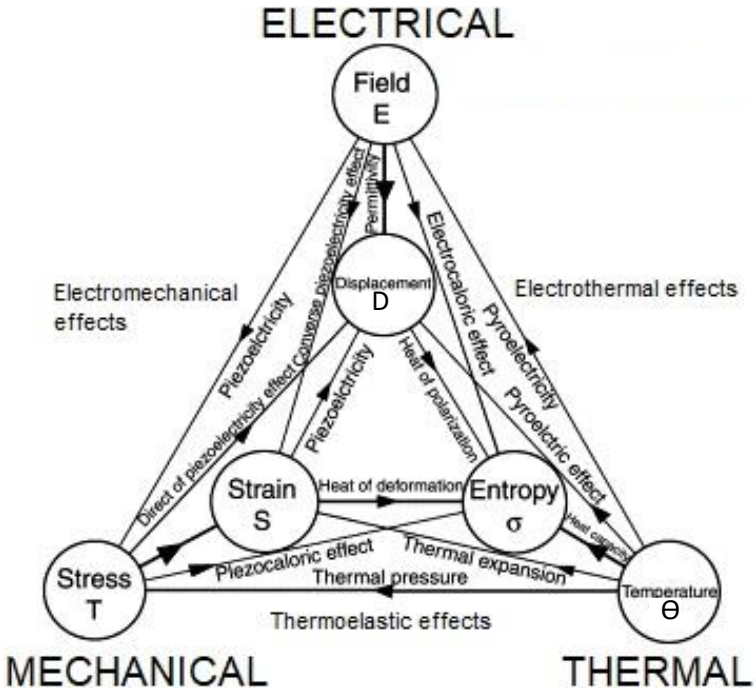

Figure 5: Heckmann's diagram showing the relation between thermal, electrical and mechanical properties (adapted from Nye, 1985:170)

Residual stress, on the other hand, is the stress that occurs in a structure deprived of the action of any external loads or stress. This type of stress develops to various intensities in the manufacturing of basically all mechanical parts. Plastic deformations, phase transformations or thermal processes, which are caused by processes such as forming, machining, cutting, heat-treating and coating, all result in residual stress (Makino, 1994:1-2).

According to Ramakrishnan (1998:9), the distribution of residual strain at any point, ε_{ijk}, can be calculated from the state of residual stress at that point, σ_{ijk}, with i=x, j=y and k=z by the following equations using the cartesian coordinate system:

$$\varepsilon_x = \frac{1}{E}[\sigma_x - \nu(\sigma_y + \sigma_z)]$$

Equation 16: Residual strain at point in x-direction

$$\varepsilon_y = \frac{1}{E}[\sigma_y - \nu(\sigma_x + \sigma_z)]$$

Equation 17: Residual strain at point in y-direction

$$\varepsilon_z = \frac{1}{E}[\sigma_z - \nu(\sigma_x + \sigma_y)]$$

Equation 18: Residual strain at point in z-direction

where:

- E is the Young's modulus of the material; and
- ν is the Poisson's ratio.

There are two types of residual stress, namely macro- and micro-residual stress. Macro residual stress acts over a large area due to plastic deformation processes, whereas, micro residual stress is distributed onto the macro stress and results from in-homogeneities within the microstructure (Makino, 1994:2).

Paradowska *et al*. (2005:1099), claim that the single largest unknown cause in industrial damage situations, is due to residual stress. In addition, residual stress is also difficult to measure. Any high residual stress is accountable for the loss of enactment in fatigue, fracture and corrosion. Paradowska *et al*. (2005:1099-1104) conducted an investigation to compare the characteristics of residual stress for a single bead weld and for different numbers of weld beads in fully restrained samples. The neutron diffraction technique was used in the study. Characterisation of the distribution of the residual stress due to the welding process of the

component, was the aim of the research. This study lead to very important significances regarding the design of welding procedures.

The net sum of all residual stresses within a component or structure remain in internal equilibrium. Thus, over any cross-sectional area, consisting of compressive stresses and tensile stresses, the resultant stresses are zero. Residual stresses in a component that are compressive of nature, are sometimes deliberately introduced in the material with the reason to improve the mechanical characteristics and/or service life (James & Buck, 2006:62; Makino, 1994:iv).

According to He (2005:77), the residual stress equilibrium condition on a cut plane of an object can be stated using the following equation:

$$\int \sigma dA = 0$$

Equation 19

on any plane section, and

$$\int dM = 0$$

Equation 20

where,

σ is the stress separated by:

$$\{\sigma\}^T = \{\sigma_{xx}\sigma_{yy}\sigma_{zz}\sigma_{xy}\sigma_{yz}\sigma_{xz}\}^T$$

Equation 21

where:

- σ_{xx}, σ_{yy} and σ_{zz} are the stress components to the normal of the x, y and z-plane;
- σ_{xy}, σ_{yz} and σ_{xz} are the shear stress components;
- A is the area; and
- M is the residual stress moment.

Stresses cannot be measured directly, but rather by means of indirect quantities such as strains or deformations. These deformations/strains are then converted to stresses (Makino, 1994:43).

Residual stresses can be determined via the following methods (Ali Fatemi-University of Toledo):

- Analytically - i.e. the local strain approach;

- Computationally - finite element analysis; and
- Experimentally - most common methods.

2.4 Residual Stress Simulation (Computational)

There are limited simulation methods to predict or determine the residual stress in materials. These methods include different finite element analyses in two- and three-dimensional configurations (Abou Msallem *et al*., 2010:108; Bonnaud & Gunnars, 2015:532; Parry *et al*., 2016:4) and specific casting related software such as MAGMASOFT® (Johnson *et al*., 2012:1488). As stated in section 1.1, the MAGMASOFT® software aims to simulate all aspects during and after the casting process and also predicts the presence of residual stress (MAGMA, 2012c).

MAGMASOFT® is used in the metal casting industry, particularly for the cast optimisation of components in heavy industry and automotive applications (MAGMA, 2012a).

The company MAGMA, which developed MAGMASOFT®, claims to be: “a world-wide leading developer and supplier of software for casting process simulation”. MAGMA states that they work actively with their customers in order to incorporate progressive technology for simulation into their processes (MAGMA, 2012a).

MAGMASOFT® is designed to forecast the total metal casting quality. This is done by simulating the filling of the mould, solidification of the material and the cooling of the material. Residual stress, distortion, property distributions and microstructure formation can also be evaluated in all cast manufacturing methods by MAGMASOFT®. Cost and different quality objectives can be pursued simultaneously by the simulation in a virtual test plan (MAGMA, 2012b).

The software can be used for enhanced process robustness and the quality of parts through the following stages (MAGMA, 2017):

- Conceptual to final component design;
- In the tooling layout and prototyping process; and
- Up to the production and heat treatment processes.

MAGMASOFT®, that is a modular software design, is said to cover cast components’ complete procedure chain. The following modules are available (MAGMA, 2017):

- MAGMAiron, MAGMAsteel and MAGMAnonferrous: *Material-specific modules - predicts microstructures, properties, consider alloys and metallurgy.*

- MAGMAhpdc, MAGMAlpdc, MAGMApermanent mould, MAGMAwheel and MAGMAinvestment casting: *Process modules - considers specific process requirements and controls manufacturing processes.*
- MAGMAc+m (core and mould) and MAGMAdielife: *Products and functionalities - predicts core shooting, purging and gassing and allows for the assessment of die life aid by making use of the best available information.*
- MAGMA HT thermal, MAGMAstress, MAGMAlink; and MAGMAdielife: *Modules for simulating heat treatment effects, machining effects and stresses within the component after the casting process.*

MAGMASOFT® and its additional modules contain the following functionalities for a complete simulation (MAGMA, 2017):

- Graphical user interface;
- Project management perspective to handle optimisation and simulation projects;
- Parametric Solid Modelling of geometries by means of a CAD kernel and the import and export of CAD data;
- Automatic meshing of geometries;
- Comprehensive process mapping which provides access to all the materials, process steps and the correspondent settings for simulation;
- Virtual design definitions and optimisation run parameters;
- Simulation programs to calculate mould filling, cooling, solidification and applications of serial casting;
- Automatic and interactive evaluation of results, editing and opening several perspectives at the same time;
- Comprehensive evaluation and visualisation result perspective of simulation results;
- Easy quantitative valuation of virtual experiment design or optimisation runs;
- Database module – for the managing of thermo-physical and other process data required by the simulation;
- Microstructure and property prediction and the consideration of metallurgy and alloys;
- Specific process requirement consideration and the controlling of the manufacturing process;
- Prediction of Core shooting, gassing, and purging prediction and die life aid assessment; and
- Stress simulation after casting, heat treatment and machining.

MAGMASOFT® can simulate the casting process of most casting materials including grey iron, die cast aluminium, steel, among many others. This software is also appropriate for all the metal casting processes by means of virtual experimentation for the duration of casting and process layout (MAGMA, 2012b).

The stress that MAGMASOFT® calculates, using the module MAGMAstress, is obtained by the conversion strain calculations. The total strain is made up of thermal and mechanical strain given by Equation 22 (Johnson *et al*., 2012:1492):

$$\varepsilon_{tot} = \varepsilon_{th} + \varepsilon_{mech} = \varepsilon_{el} + \varepsilon_{pl} + \varepsilon_{th}$$

Equation 22: Total strain equation

where:

- ε_{tot} is the total strain;
- ε_{th} is the thermal strain;
- ε_{mech} is the mechanical strain;
- ε_{el} is the elastic strain; and
- ε_{pl} is the plastic strain.

The temperature history is used to calculate the thermal strain increments and is integrated over time throughout cooling. The thermal strain also includes volumetric expansion and contraction is also included in the thermal strain which is obtained from the phase transformations and is given by Equation 23 (Johnson *et al*., 2012:1493).

$$\varepsilon_{th} = \int_{t_2}^{t_1} \alpha(T) dT$$

Equation 23: Thermal strain equation

where:

- T is the temperature; and
- α is the thermal expansion coefficient.

MAGMASOFT® uses the following elasto-plastic formulation based on a combination using Hooke's Law – see Equation 24 (Johnson *et al*., 2012:1493):

$$\sigma_{ij} = \frac{E}{1+\nu}\left(\varepsilon_{ij} + \frac{\nu}{1-2\nu}\delta_{ij}\varepsilon_{kk}\right) - \delta_{ij}\frac{E\alpha\Delta T}{1-2\nu}$$

Equation 24: Elasto-plastic formulation based on Hooke's Law

where:

- δ_{ij} is the Kronecker delta;
- ε_{kk} is the strain tensor; and
- A temperature-dependent yield condition, with isotropic hardening is given by a classical J2 formulation in Equation 25.

$$\varepsilon_{mech} = \begin{cases} \frac{\sigma}{E} & for.....\sigma \prec \sigma_y \\ \frac{\sigma_y}{E}\left[\frac{1}{n}\left(\frac{\sigma}{\sigma_y}\right)^n - \frac{1}{n} + 1\right] & for.....\sigma \geq \sigma_y \end{cases}$$

Equation 25: Mechanical strain equation

where:

- n is the hardening parameter; and
- σ_y is the yield stress.

The following, should also be noted:

- This kind of plasticity is volume preserving, thus all the changes in density are in the elastic model; and
- Time effects such as viscoplasticity, creep, and general rate effects, aren't considered for the purposes of these calculations.

2.5 Residual Stress Determination (Experimentally)

There are various techniques for experimentally measuring residual stress. The two main categories are destructive and non-destructive. Destructive techniques include hole drilling, dissectioning, among others. Non-destructive techniques include X-ray diffraction, neutron diffraction, magnetic methods and ultrasonic measurement (James & Buck, 2006:62; Paradowska *et al*., 2005:1099; Webster & Wimpory, 2001:395).

In this study, a short description will be given of two destructive methods namely, hole drilling and dissectioning; as well as three non-destructive methods that were reviewed in more detail, namely ultrasonic measurement, neutron- and X-ray diffraction.

2.5.1 Strain gauges (Hole Drilling)

The hole drilling method is accomplished by mounting a rosette gauge at the desired point to be measured for residual stresses. A mill is used, which is firmly guided, to directly drill a hole in the centre of the rosette gauge's three elements (Ramakrishnan, 1998:24).

Due to the removal of the material, surface relaxation occurs. Strains are then created which are used to determine the residual stresses. This method is considered as semi-destructive, and not completely destructive, due to the following two reasons (Ramakrishnan, 1998:25):

- As a result of the tiny drilled hole (usually 1.5 - 3.0 mm in depth and diameter).
- The object on which the measurement is done, can occasionally be returned to service.

The hole drilling method is analytically and experimentally quite simple and the equipment required is commercially available and relatively inexpensive. Hole drilling is, however, limited to flat surfaces and only near-surface residual stress distribution information can be provided (Paradowska *et al*., 2005:1099; Ramakrishnan, 1998:25).

2.5.2 Dissectioning

This method requires components to be dissected into layers. The residual stress distribution throughout the body can be determined by the following:

- Measuring the deformation in each layer;
- Measuring the curvature of the remaining material; or
- Measuring the distortion of the remaining material.

A redistribution of internal strains occurs as each layer is cut away to uphold static equilibrium. The result is deformation, created by the redistribution of the strains, which may then be used to calculate the stresses within the part (Ramakrishnan, 1998:25).

This method is accurate, although it is time consuming and fairly difficult to utilise in practice. The stress distribution is only approximated from the stresses within each layer sampled throughout the volume of the part. The accuracy can only be obtained by this method's time-consuming testing of several identical parts. Dissectioning is best suited for situations where large quantities of parts are produced by repeatable and well-controlled processes (Ramakrishnan, 1998:25).

2.5.3 Ultrasonic Residual Stress Measurements

This technique makes use of acoustic waves that spread within the stressed material and can measure near-surface and bulk stresses. The ultrasonic waves used, is not enough to damage the material measured, thus ensuring this technique to be non-destructive. The required equipment needed for this method is said to be relatively inexpensive when compared to other methods and can be portable. The acoustic acquisition equipment used, must be able to

measure highly accurate travel time with precision in the order of 0.025 µs or higher (Ramakrishnan, 1998:33).

The anharmonicity of the inter-atomic potential is the physical foundation for stress measurements by ultrasound. When a stress is applied to a solid (on a microscopic basis), a change in the inter-atomic distance is primarily caused which produces a change in the velocity of sound.

A method for obtaining initially stress-free metals' elastic modulus can be achieved by the measurement of the velocity of ultrasonic waves. This is based on the submission of small levels of stress to a metal which changes ultrasonic waves' velocities in the material, yielding a linear relationship between the change in the velocity and the applied stress (Ramakrishnan, 1998:33).

When there is a linear relationship between the elastic strain in the material and the acoustic wave speed, it is referred to as acoustoelasticity. The effect acoustoelasticity has on ultrasonic velocities is fairly small (in the order of a few hundreds of a percent). Nevertheless, it has been used successfully for many years to measure near-surface and bulk stresses.

The magnitude and nature of the acoustoelastic response is dependent on the material and the type of ultrasonic wave, for example, shear or longitudinal. The acoustoelastic factor is referred to as the materials' (with a given microstructure) magnitude of response to stress. The acoustoelastic factor, which is dimensionless, is the ratio of the normalised change wave velocity and the materials' strain is shown by the following (Ramakrishnan, 1998:34):

$$AEC = \frac{\left(\frac{\Delta v}{v_0}\right)}{\Delta \varepsilon}$$

Equation 26: Acoustoelastic factor equation

where:

- AEC is the acoustoelastic constant $\Delta v = \left(v - v_0\right)$;
- v is the stressed condition ultrasonic wave velocity; and
- v_0 is the ultrasonic wave velocity in the stress-free condition of the material.

The following equation can be used to determine the estimate residual stress levels (Ramakrishnan, 1998:35):

$$\sigma = \frac{E}{-(AEC)t}(t - t_0)$$

Equation 27: Residual Stress Equation using the Acoustoelastic Constant

where:

- E is the Young's Modulus;
- t measured stressed state travel time; and
- t_0 stress free travel time.

2.5.4 Neutron and X-ray Diffraction

Neutron diffraction is a relatively new method, in comparison to X-ray diffraction, for the analysis of multi-axial residual stress. The main reason why neutron diffraction is a relatively new concept, is because of the comparatively low availability of neutron sources in comparison with X-rays. The intensity of the most powerful neutron sources, available up to 1983, were still numerous times lower in magnitude in comparison with the intensity of common X-ray tubes. In addition, Pintschovius *et al*. (1983:43) states that structure analysis experiments, by means of neutron diffraction, can be performed at lower source intensities than X-rays.

Neutron diffraction is similar to X-ray diffraction, except, instead of the use of X-rays which interact with the electron cloud, neutrons are used to interact with the nucleus. Pintschovius *et al*. (1983:44) states that a neutron beam attenuates to half of its original intensity at the depth of 6 mm in steel or 70 mm in aluminium. These values are approximately three orders of magnitude larger than the equivalent values for those of X-rays.

To attain stresses through the thickness of a part, special etching methods are needed when using laboratory X-ray sources. Without the etching, only surface measurements are possible. Both high-energy synchrotron X-ray diffraction and neutron diffraction are capable of measuring internal stresses of a part by penetrating through the thickness thereof (Johnson *et al*., 2012:1487).

Neutron diffraction has an exceptional ability to obtain residual stress, known to be non-destructive, within the inner parts of components. This can be accomplished in three dimensions, in minor test volumes to an extent as small as 1 mm^3 and in thick specimens, up to several cm^3 (Paradowska *et al*., 2005:1100).

As in the stress analysis of X-ray diffraction, the stress analysis of neutron diffraction is also based on the lattice strain determination. This is done by precise measurements of the d-spacing's in a sample's different directions. The d-spacing's (d) are then converted to strain

where after the strain is converted to stress. In Figure 6 a schematic diagram of a typical layout of a neutron diffraction instrument, is shown.

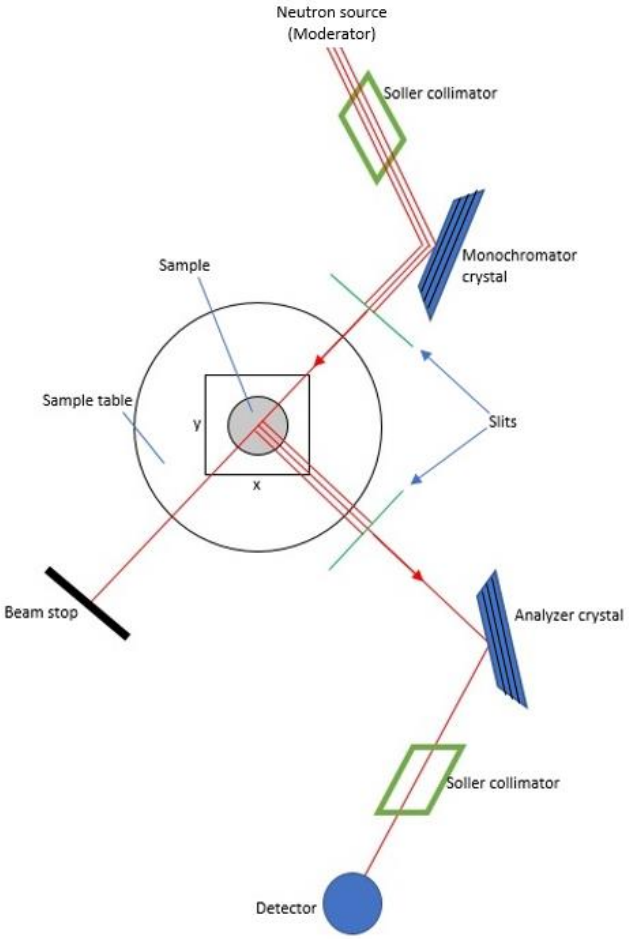

Figure 6: A schematic diagram of a typical layout of a neutron diffraction instrument showing the sample at coordinates x and y (as adapted from Pintschovius *et al*., 1983:44)

2.6 Principles of Neutron Diffraction

By exposing a beam of neutrons with a wavelength λ to a crystalline material, a diffraction pattern is produced with some sharp maxima. The Bragg equation gives the angular positions of this maxima for a group of crystallographic planes with separation of d_{hkl} (Webster & Wimpory, 2001:365).

The Bragg equation is as follows:

$$n\lambda = 2d_{hkl}\sin\theta_{hkl}$$

Equation 28: Bragg's equation

where:

- n is an integer number that represents the reflection plane's order; and

- $2\theta_{hkl}$ is the diffraction angle.

There are two types of neutron beams that can be used, namely a pulsed polychromatic beam or a continuous monochromatic beam (Webster & Wimpory, 2001:365).

A change in a lattice spacing, Δd, will cause an equivalent angular shift, $\Delta\theta$, by means of the Bragg reflection. The lattice normal strain within the direction of the Q vector (see Figure 7), is provided by the following equation (Webster & Wimpory, 2001:365):

$$\varepsilon = \frac{\Delta d}{d_0} = \frac{d - d_0}{d_0} = -\Delta\theta \cot\theta$$

Equation 29: Lattice strain equation

where:

- d_0 is the strain free lattice spacing; and
- θ is the diffraction angle of the unrestrained lattice spacing.

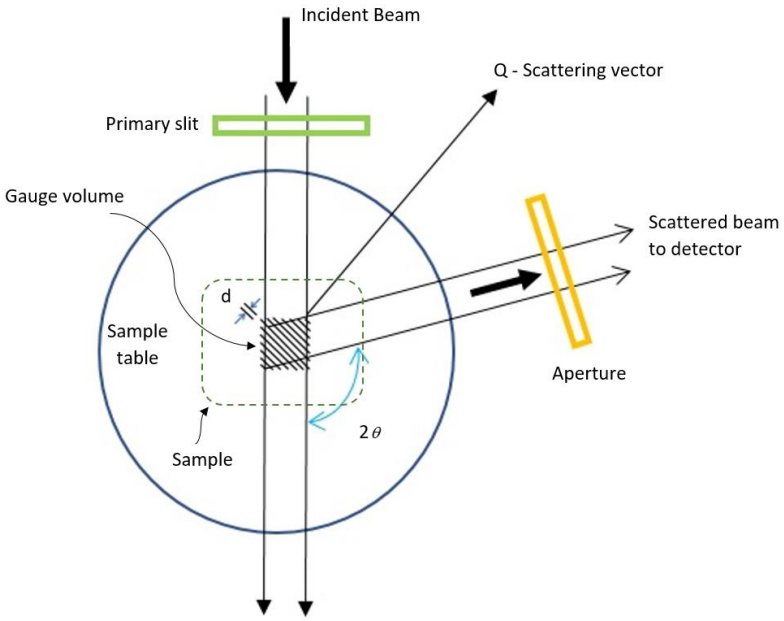

Figure 7: A basic diagram showing the Q – scattering vector direction normal to the plane (adapted from Webster & Wimpory, 2001:369)

By applying the method which uses the continuous monochromatic beam, a single peak profile is studied and the angular position is determined using a Gaussian/Lorentzian fitting routine (Figure 8). For this single peak analysis, the specific appropriate (hkl) crystallographic plane values are used for the measurement of the strain.

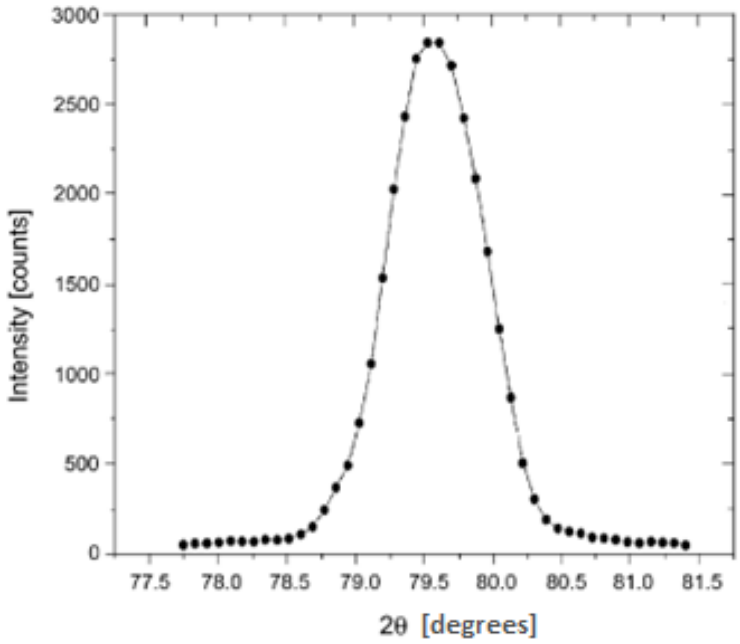

Figure 8: An example of a neutron single peak profile of an unknown material (adapted from Webster & Wimpory, 2001:369)

The uncertainty (standard deviation values) of the peak position fittings are spread throughout the calculations of the stress error determinations. The strain error is calculated by means of Equation 30 (Marais *et al.*, 2016:33).

$$Err(\varepsilon)^2 = \frac{Err(d)^2}{d^2} + \frac{Err(d_0)^2}{{d_0}^2}$$

Equation 30: Strain error equation

where:

- $Err(d)$ and $Err(d_0)$ are individual quantities in the peak measurement of d and d_0.

A full diffraction spectrum (Figure 9) can be generated when a change in the time-of-flight of the neutrons between the detector and the moderator is recorded. This is possible when an intermittent beam with an array of wavelengths, is employed and the measurements take place at a repeated scattering angle, normally $2\theta = 90°$ (Webster & Ezeilo, 1997:950; Webster & Wimpory, 2001:395).

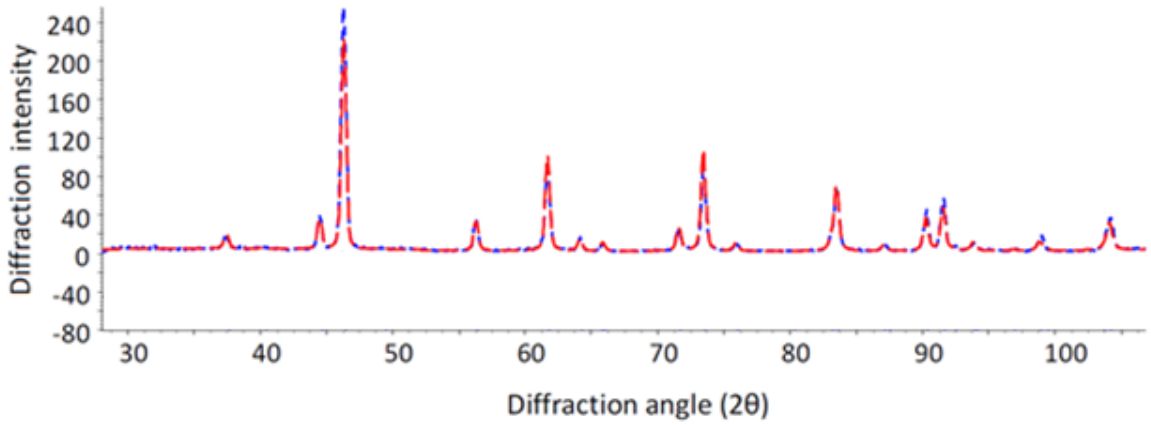

Figure 9: Example of a diffraction spectrum pattern of Al_2O_3 (adapted from Marais, 2016:71).

By applying a Rietveld refinement to the spectrum or analysing the individual peaks, strain can be determined. In order to do this, the d_0 value (zero stressed lattice spacing), calculated from the $2\theta_0$ value (scattering angle), must be known. Measurements in three or six orientations are required, depending if the principal directions are known, to define the stress tensor (Webster & Ezeilo, 1997:950; Webster & Wimpory, 2001:395).

The principal stresses are given by the following equations (Webster & Ezeilo, 1997:950):

$$\sigma_x = \frac{E}{(1+v)(1-2v)}[(1-v)\varepsilon_x + v(\varepsilon_y + \varepsilon_z)]$$

Equation 31: Principal stresses in the x-direction

$$\sigma_y = \frac{E}{(1+v)(1-2v)}[(1-v)\varepsilon_y + v(\varepsilon_x + \varepsilon_z)]$$

Equation 32: Principal stresses in the y-direction

$$\sigma_z = \frac{E}{(1+v)(1-2v)}[(1-v)\varepsilon_z + v(\varepsilon_x + \varepsilon_y)]$$

Equation 33: Principal stresses in the z-direction

In these equations v is Poisson's ratio and E is the elastic modulus of the material.

2.7 Neutron Diffraction Instrumentation Facilities

In South Africa, the only available neutron diffraction facility is located at the South African Nuclear Energy Corporation (Necsa) SOC Limited, SAFARI-1 research reactor, which

comprises of two instruments: MPISI (Materials Probe for Internal Strain Investigations) and PITSI (Powder Instrument for Transition in Structure Investigations) (Marais & Venter, 2017).

The MPISI instrument is said to be competitive with similar leading international facilities' instruments. Measurement of complex multi-dimensional strain maps of samples, while the neutron beam utilisation is optimised, is possible by means of the following (Marais & Venter, 2017):

- State-of-the-art data acquisition;
- Control; and
- Analyses systems.

The samples can be positioned within an accuracy of 10 µm by means of using micro-stepping in conjunction with surface scans (Marais & Venter, 2017). The technical data of the MPISI instrument is provided below in Table 2.

Table 2: MPISI Material Science Neutron Diffraction Instrument – Technical Data (adapted from Marais & Venter, 2017).

Monochromator	Double focussed bent perfect Si crystal
Wavelength	1.49 and 1.67 Å
Beam Size	Manually adjustable: - 0.3 - 5 mm horizontal - 0 - 20 mm vertical Radial collimators: 1, 2, 3, 10 mm
Detector	Denex-300TN ^{3}He filled 300 mm (hor.) x 300 mm (ver) Range: 10° ≤ 2Θ ≤ 110°
Sample Stage	Huber integrated XYZ Maximum sample weight: 250 kg XYZ Linear travel: 250 mm ⅓ cradle with integrated ϕ, χ, XYZ
Sample Mounting	Various chucks, CNC machine vices etc.
Flux at Sample Position	10^{6} neutrons $cm^{-2}s^{-1}$

2.8 Effects of Heat Treatment on Residual Stress

Residual stress is directly related to how the heat was controlled during casting and how the heat will be controlled during heat treatment in a casting. Expansion and contraction, and the relation between stress and strain (residual stresses) are affected by the temperature and

temperature distributions in the casting. Thus, by controlling the heat input, phase transformations and shrinkage of a casting, residual stress can also be partially controlled (Paradowska *et al*., 2005:1099).

Heat treatment is an important and useful tool for improving both the uniformity and range of the properties of steel and, more specifically, ductile iron castings to a higher extent of those produced in the as-cast condition (Shekhar & Jaiswal, 2008:1; Warda, 1990:7-1).

Heat treatment can be performed to achieve the following results (Warda, 1990:7-1):

- Increase toughness and ductility;
- Increase strength and wear resistance;
- Increase corrosion resistance;
- Stabilise the microstructure, to minimise growth;
- Equalise properties in castings with widely varying section sizes;
- Improve consistency of the properties;
- Improve machinability; and
- Relief of internal stresses.

The relief of stress by means of heat treatment is achieved by heating the casting to a certain high temperature for the strength to be reduced to the level for the residual stress to be relieved by plastic deformation (Cañas *et al*., 1996:736; Warda, 1990:7-3). Numerous factors influence the extent to which the residual stress is relieved/eliminated. These factors include the following (Warda, 1990:7-13):

- Residual stress severity;
- Stress relieving time;
- Stress relieving temperature;
- The heating-cooling cycle; and
- The composition and microstructure.

In Figure 10, it is shown that stress relief is proportional to the initial level of stress and the degree of stress relief is strongly dependant on the temperature.

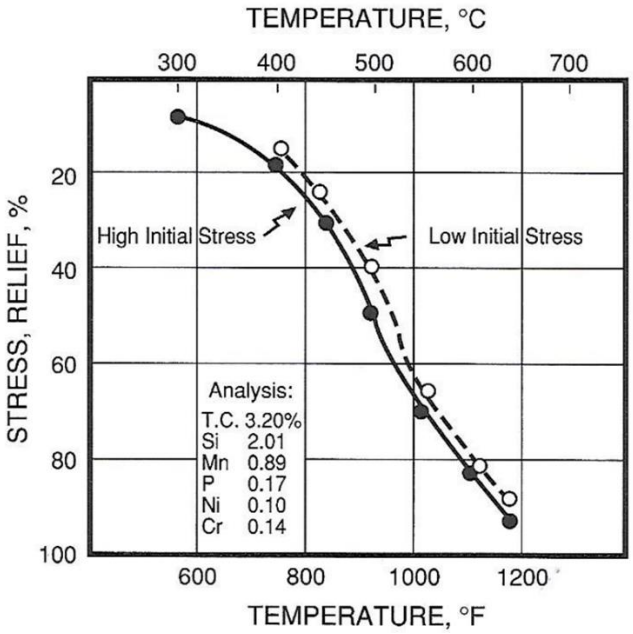

Figure 10: The effect of initial stress level and stress relieving temperature on the percentage of stress that is relieved in 1 hour at the indicated temperature (adapted from Warda, 1990:7-14).

Applying a uniform cooling rate throughout the casting, is of most importance to prevent the reintroduction of stresses. According to Warda (1990:7-15), for complex castings where the greatest degree of stress relief is desired, furnace cooling of up to 150 ˚C, is required.

According to the Dura-Bar Heat Treating Guide (Dura-Bar, 2016), a heat treat cycle for the relief of stress is as follows:

- Heat to 800-1100 F (426-600 ˚C);
- Hold for 1 hour per inch cross section;
- Furnace cool to 300 F (148 ˚C); and
- Air cool to room temperature.

2.9 Effects of Machining on Residual Stress

Machining can cause residual stress to increase or decrease. This is all dependant on the following (Zhang *et al*., 2016:182):

- Tool geometry;
- Material properties;
- Machining parameters; and
- Amount of material removal.

The change of cutting slate and the effect on residual stresses can be resultant due to the following factors (Zhang *et al*., 2016:182):

- The vibration of the machine tool and the machine – can possibly lead to changes of immediate cutting speed and depth.
- Tool wear - can possibly cause the tool edge geometry to change, thus influencing the temperature, cutting forces and stress distribution applied on the specimens.

It was reported in a study completed by Zhang *et al*. (2016:182) that, due to material removal, there was large variation in surface residual stress. It was also found that tool sharpness had the greatest effect on residual stresses in the machining of 304 austenitic stainless steel.

2.10 Conclusion

It is evident from the literature that the presence or absence of residual stress can have a major influence in ductile iron castings. Therefore, it is extremely important to be able to determine the amount and intensity of residual stresses in castings to verify whether or not negative influencing residual stresses are present, in order to prevent premature failure.

According to the literature, MAGMASOFT® is one of the most advanced cast process simulation software packages on the market. This software could be verified by means of several methods, although only a few methods are non-destructive.

One of the non-destructive methods, namely neutron diffraction, is more advantageous than the rest. This is mainly because it can penetrate the deepest within the components measured to determine the residual stress. Another advantage is the fact that a neutron diffraction facility is available for research purposes.

It is also evident that heat treatment plays a big role in the relieving of residual stresses within a component that is cast. When considering the effect that machining has on residual stress, it is evident that several factors can have an influence on the increasing or relieving of residual stress.

3. RESIDUAL STRESS SIMULATION

3.1 General

Due to the geometric complexities associated with valves and high costs thereof, a tree consisting of simple cylindrical shaped branches (Figure 11) was used for this investigation and verification exercise. The reason for the use of the tree was due to financial implications and limitations in terms of the physical casting of the tree (discussed in section 4.1).

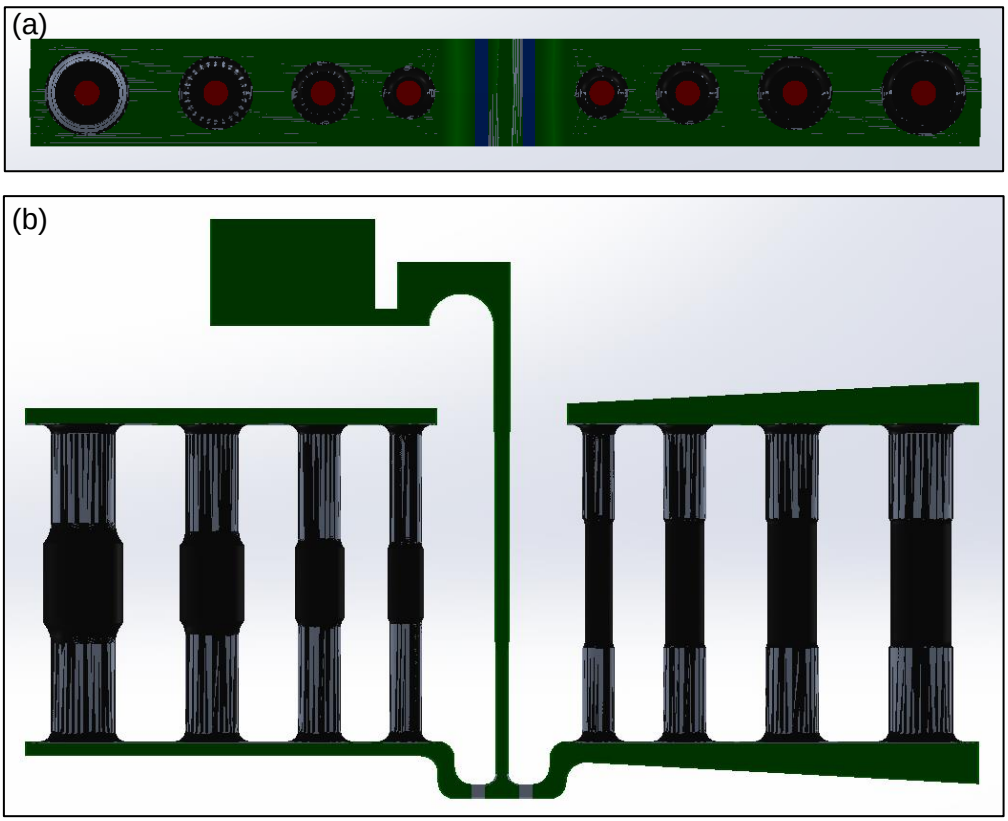

Figure 11: (a) Sectional cut top view showing the cylindrical branches' diameters and (b) front view of the 3D model ductile iron cast tree

The tree was designed according to the Birmingham UK 10 test bar (see Figure 12) and modified to represent valve bodies as close as possible according to its geometrical relations. This basic design allows the liquid metal filling of the mould to be controlled via the runners and also maximises the filling process repeatability (Combrinck, 2017:47).

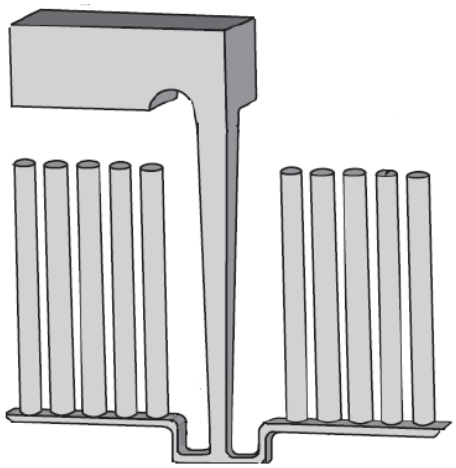

Figure 12: Schematic illustration of the Birmingham UK 10 test bar configuration (adapted from Combrinck, 2017:48)

The representation of the valve bodies can be explained according to the following (Combrinck, 2017:47):

- The thinnest sections in typical valve bodies are usually the inlet walls of the valves with a thickness of about 5 - 10 mm. The thickest sections are usually the flange connections with a typical thickness of between 20 - 30 mm for PN16-DN400 valves (mentioned as an example), typically used in water distribution networks in South Africa. The test samples range in thickness from 15 to 30 mm (base diameter) with steps of 5 mm (thus 4 test samples on each side of the tree) to represent a range of different wall thicknesses present in valve bodies.

- Thickened centres have been included to represent areas which increase in thickness in valves. These areas are prone to shrinkage usually due to poor feeding which can induce residual stresses. Similar thinned out centres were included as seen in Figure 11.

- To represent the flanges in valves, different thickness flanges have been added as upper and lower runners of the castings that represent the flanges of a valve, which also may induce residual stress.

- Fillets were inserted into all sharp corners to replicate the actual valves.

The cast tree shown in Figure 11 consists of eight cylindrical branches with different diameters (15-30 mm at base), a pouring basin, sprue and a runner. The branches were modelled and simulated using MAGMASOFT®. The residual stress values in the branches were then extracted.

The simulation was accomplished by means of importing a 3D model of the tree, created in Solidworks (3D Cad Design Software), into MAGMASOFT®. All the casting features and variables, for example the inlet, pouring basin, runner, heat treatment, machining, liquid metal temperatures, among others were selected (to be discussed below) in MAGMASOFT® in order to run the simulation.

Three simulations were run on the branches and are listed below:

1. Branches without runners - Simulation (V2);
2. Branches without runners and subjected to heat treating - Simulation (V3); and
3. Branches without runners and subjected to machining - Simulation (V4).

(Note: The reason why the simulations start at (V2) is due to the fact that simulation (V1) was an alternative setup/test simulation and did not form part of this report.)

The branches were simulated to be subjected to the heat treatment process and machining (also to replicate actual valve bodies which sometimes undergo these processes) to determine if residual stresses are relieved or not, as found in the literature (section 2.8 and 2.9).

The following boundary conditions were selected/used to be able to complete the MAGMASOFT® simulation:

- A liquid metal pouring temperature of 1400 °C.
- A shakeout temperature of 500 °C - this is the temperature at which the casting was simulated to be removed from the sand mould.
- After the shakeout, the casting was simulated to be air cooled to room temperature.
- A Furan resin silica sand mould was used with a heat transfer coefficient as presented in Table 3
- A pouring height of 30 mm.
- An inlet size of 24 mm diameter.
- A pouring time of 13 seconds.

The heat treatment cycle boundary conditions simulated to be subjected to the branches, obtained from the literature, were selected and are as follows:

1. The branches were heated to 600 ˚C over a period of 30 minutes;
2. Kept at 600 ˚C for one hour;
3. Furnace cooled to 150 ˚C over a period of 4.5 hours; and
4. Air cooled to room temperature.

The machining boundary conditions simulated to be subjected to the branches were directly imported from the 3D CAD model into MAGMASOFT®. A detailed drawing of the machined samples can be viewed in Appendix A.

A summary of the simulation boundary conditions is listed in Table 3.

Table 3: MAGMASOFT® Simulation Boundary Condition Summary

Simulation Boundary Conditions	
Pouring temp.	1400 [°C]
Shakeout temp.	500 [°C]
Pouring height	30 [mm]
Mould sand	Furan Sand
Mould sand heat coefficient	0-600 [°C] – 300 [W/m2K]
	600-1100 [°C] – 300 [W/m2K]
	1100-1200 [°C] – 300 [W/m2K]
	1200-2000 [°C] – 300 [W/m2K]
Inlet size diameter	24 [mm]
Pouring time	13 [sec]
Machining size	Length: 120 [mm]
	Diameter: 11.8 - 8 - 11.8 [mm]
Heat treatment	1. Heated to 600 [°C] over 30 [min]
	2. Kept at 600 [°C] for 60 [min]
	3. Furnace cooled to 150 [°C] over 270 [min]
	4. Air cooled to room temperature

EN-GJS-400 (also known as EN-JS1020 or equal to SANS SG42 ductile iron) ductile cast iron was used as the material in the simulation, this material is commonly used in the valve and piping industry in South Africa (McFarlane, 2016).

3.2 Simulation Results

The residual stress simulation results were extracted in the middle (in the cores of the cylindrical branches) of the simulated casting (see Figure 13). The section line presented in Figure 13, indicates the middle of the casting; thus, also the symmetrical line.

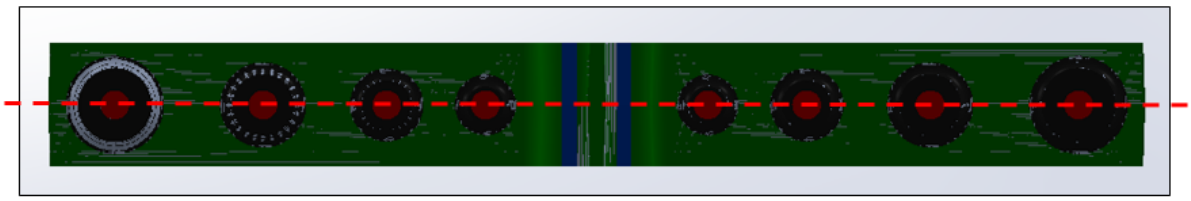

Figure 13: Section line in the middle of the casting where the results were extracted, shown on the top view of the 3D model ductile iron cast tree

In Figure 14, Figure 15 and Figure 16 the x-, y- and z-component residual stress results of simulation (V2) are presented. Note that the results were obtained in the middle of the tree as illustrated in Figure 13 and presented in the xz-plane.

The position of the maximum residual stress in the branches (determined by the maximum z-component residual stress as in Figure 16) is given in the form of labels presented on the figures and summarised in tables accordingly.

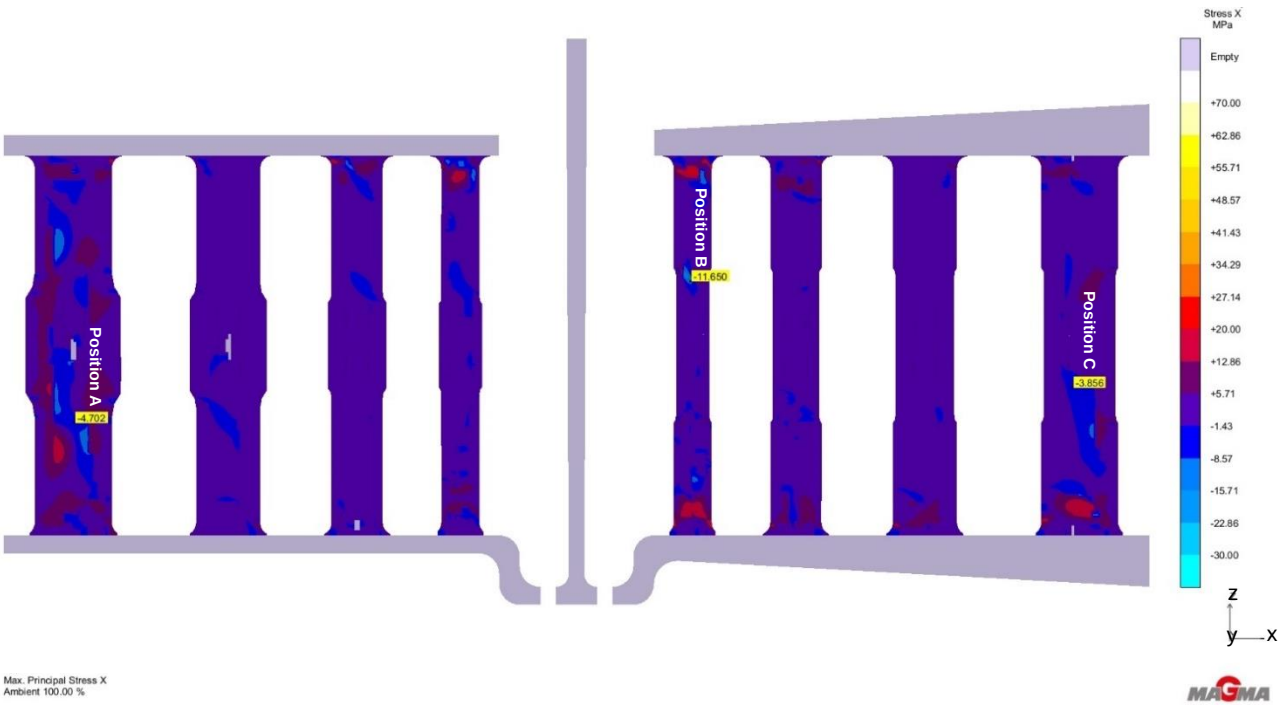

Figure 14: MAGMASOFT® X-component residual stress results – Simulation (V2)

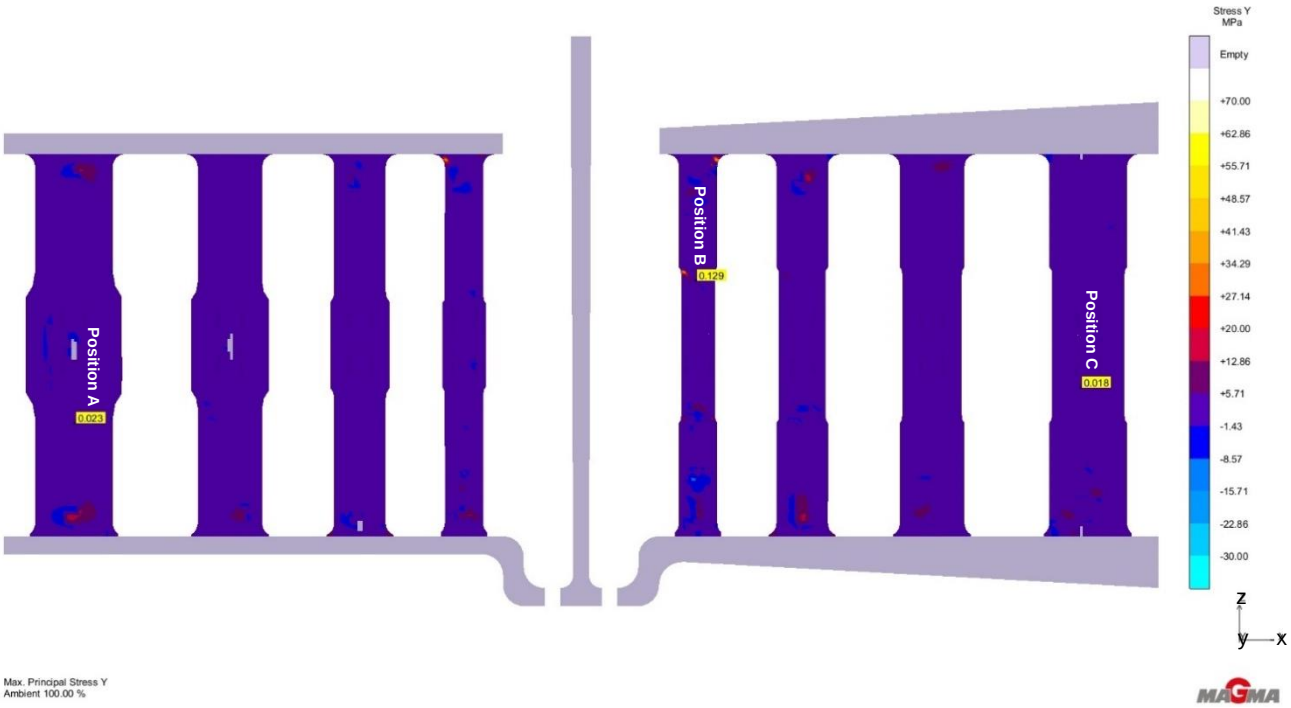

Figure 15: MAGMASOFT® Y-component residual stress results - Simulation (V2)

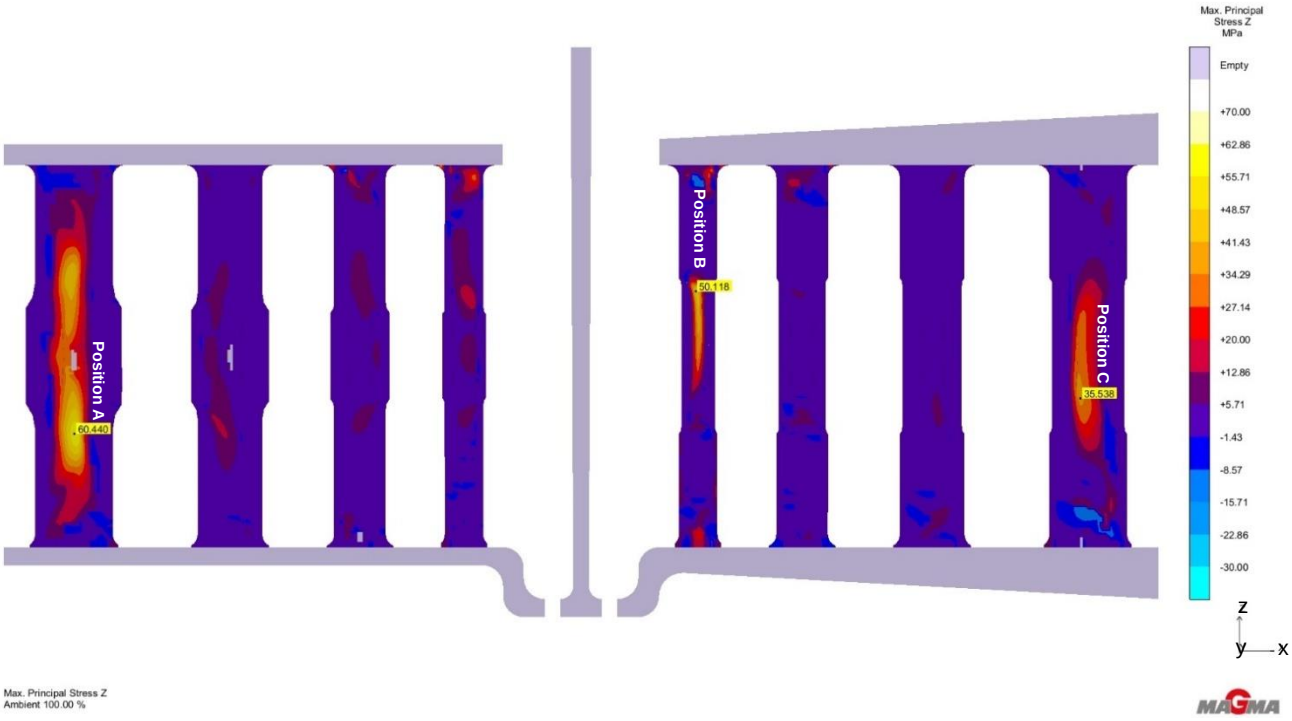

Figure 16: MAGMASOFT® Z-component residual stress results - Simulation (V2)

In Table 4 below, the maximum residual stress results of simulation (V2) are presented (Figure 14 - Figure 16). Note that the positive values are tensile residual stresses and the negative values, compressive residual stresses.

Table 4: MAGMASOFT® maximum residual stress values - Simulation (V2)

Branches without runners - Simulation (V2)			
Max Residual Stress	Position A	Position B	Position C
X – Component (Figure 14)	-4.70 MPa	-11.65 MPa	-3.86 MPa
Y – Component (Figure 15)	0.02 MPa	0.13 MPa	0.02 MPa
Z – Component (Figure 16)	60.44 MPa	50.12 MPa	35.54 MPa

In Figure 17, the simulated z-component residual stress results of the heat-treated samples simulation (V3) are presented.

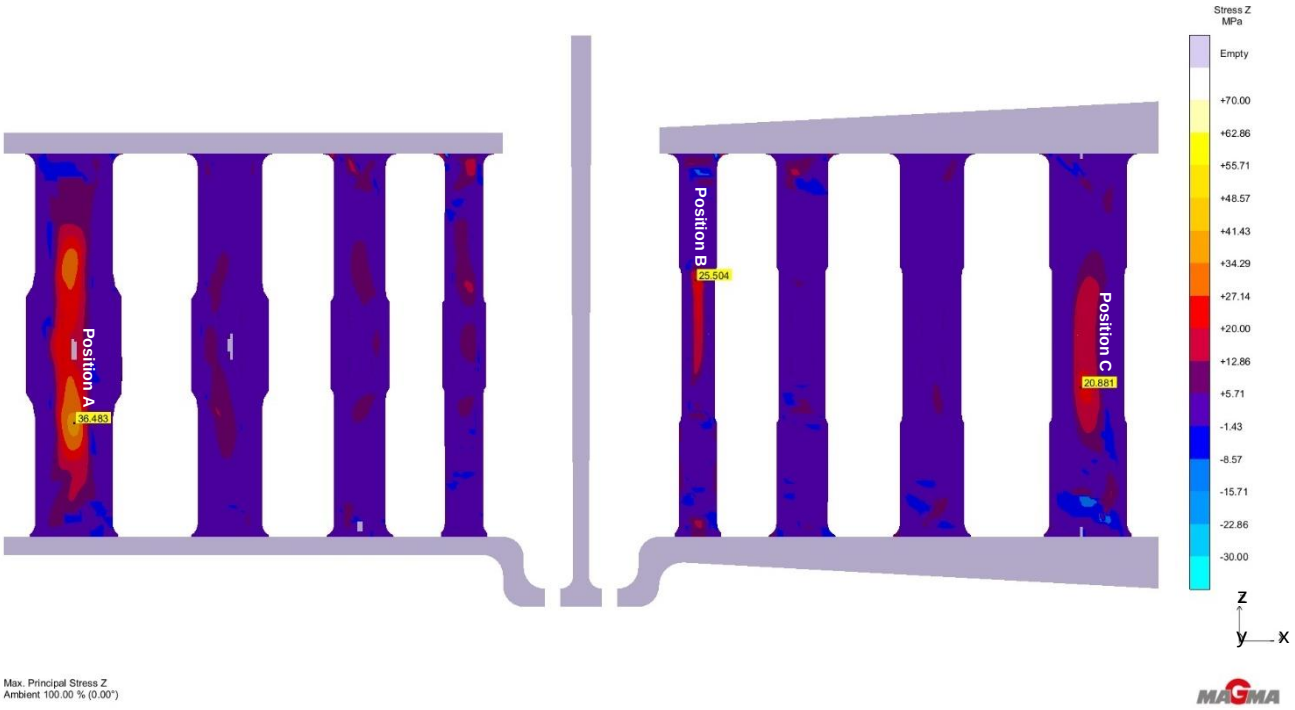

Figure 17: MAGMASOFT® Z-component residual stress results - Simulation (V3)

In Table 5 below, the maximum residual stress results, at the positions shown in Figure 17, are presented according to simulation (V3).

Table 5: MAGMASOFT® maximum residual stress values - Simulation (V3)

Branches without runners and subjected to heat treating - Simulation (V3)			
Max Residual Stress	Branch A	Branch B	Branch C
Z – Component (Figure 17)	36.48 MPa	25.50 MPa	20.88 MPa

In Figure 18, the simulated z-component residual stress results of machined samples simulation (V4) are presented.

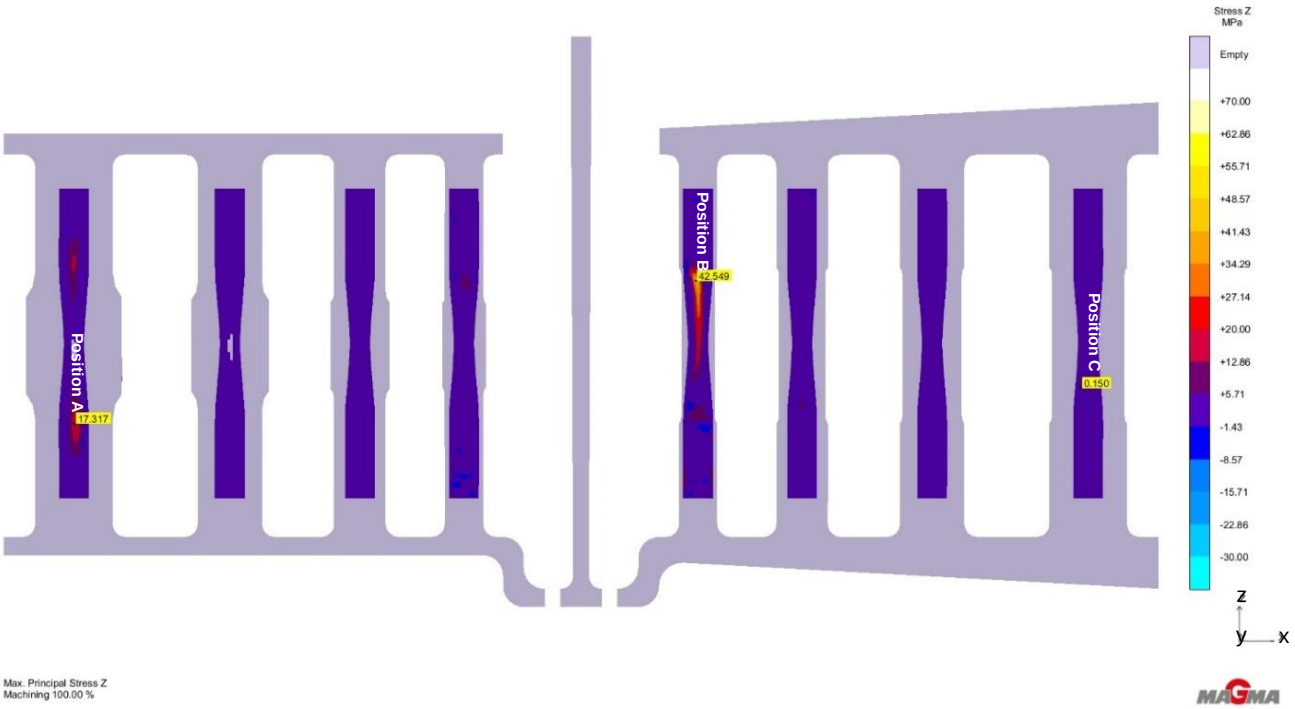

Figure 18: MAGMASOFT® Z-component residual stress results – Simulation (V4)

In Table 6 below, the maximum residual stress results, at the positions shown in Figure 18, are presented according to simulation (V4).

Table 6: MAGMASOFT® maximum residual stress values – Simulation (V4)

Branches without runners and subjected to machining - Simulation (V4)			
Max Residual Stress	Branch A	Branch B	Branch C
Z – Component (Figure 18)	17.32 MPa	42.55 MPa	0.15 MPa

3.3 Discussion

By studying the results presented in Table 4, it was noticed that the z-component residual stress results were much higher than those of the x- and y-component residual stress results.

The reason for this may be due to several factors such as the shape of the casting, how the casting filled up and solidified, the cooling down period, among others. A more precise explanation for the much higher residual stresses of the z-component, in comparison with those of the x- and y-components' residual stress results, is due to the flanges (in this case also the runners) at the top and bottom of the casting. The flanges possibly cooled down at different rates, is a different shape, and possibly solidified at different time intervals than the branches; thus, causing higher residual stresses in certain directions (in this case the z-component direction).

It was also noticed that there were three branches that stood out regarding z-component maximum residual stresses when studying Figure 16. The three branches that were simulated to have the highest resultant residual stresses are pointed out in Figure 19 below.

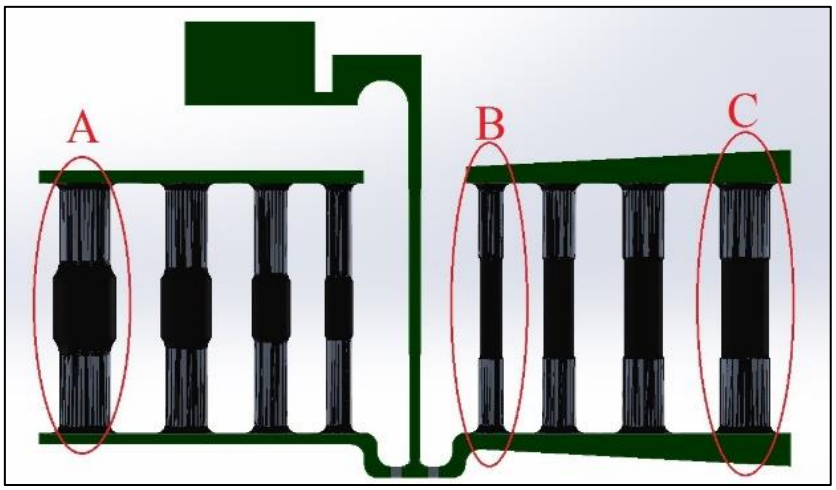

Figure 19: Branches A, B and C shown on the front view of the ductile iron cast tree 3D model, which MAGMASOFT® predicted to have the highest level of residual stress

Taking into consideration Table 4, it was decided to focus on and present only the residual stress results of the z-component.

By studying the results presented in Table 4, Table 5 and Table 6, a decrease in residual stress of the simulation results was observed when the heat treatment and machining was applied (see Table 7).

Table 7: Summarised z – component residual stress simulation results

Z – Component residual stress comparison (Figure 16 - Figure 18)			
Max Residual Stress	Position A	Position B	Position C
Branches without runners (Figure 16)	60.44 MPa	50.12 MPa	35.54 MPa
Branches subjected to heat treatment (Figure 17)	36.48 MPa	25.50 MPa	20.88 MPa
Branches subjected to machining (Figure 18)	17.32 MPa	42.55 MPa	0.15 MPa

It was also noticed that MAGMASOFT® predicted that there would be cavities present in the casting as illustrated in Figure 20 below. This will further be discussed in section 4.2. It is important to note that Branch A was predicted to have the largest cavity.

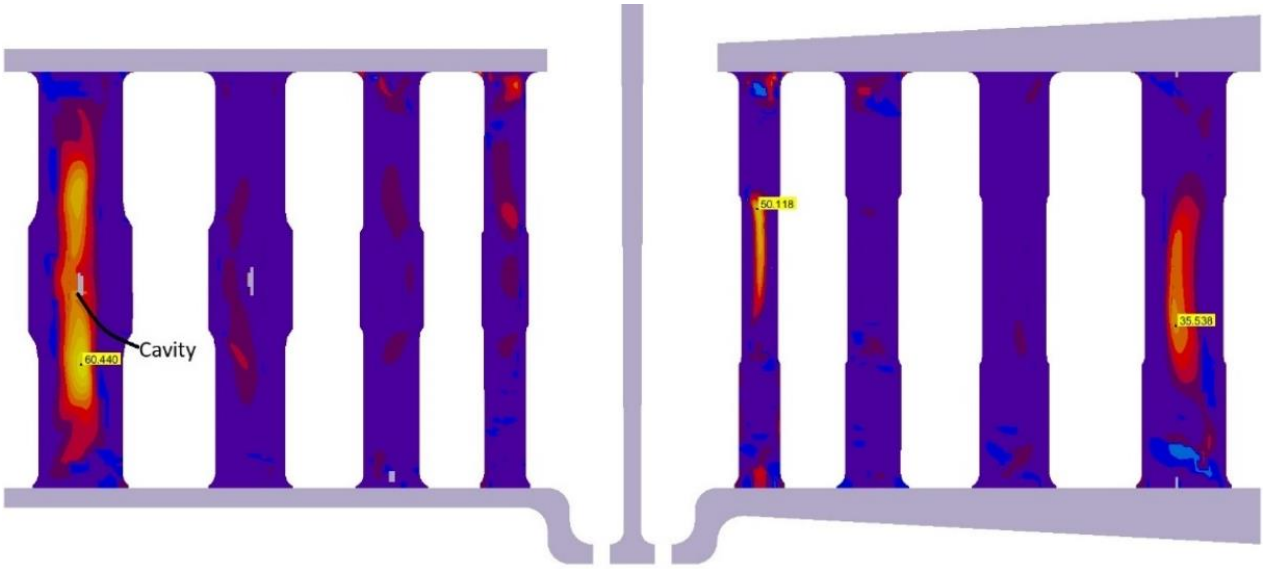

Figure 20: Predicted cavity shown, obtained from MAGMASOFT®

The MAGMASOFT® results were chosen to be verified, by means of neutron diffraction, where the simulation results predicted the highest residual stresses. The lines along which the maximum residual stress results as predicted by the MAGMASOFT® simulation, are illustrated in Figure 21 below.

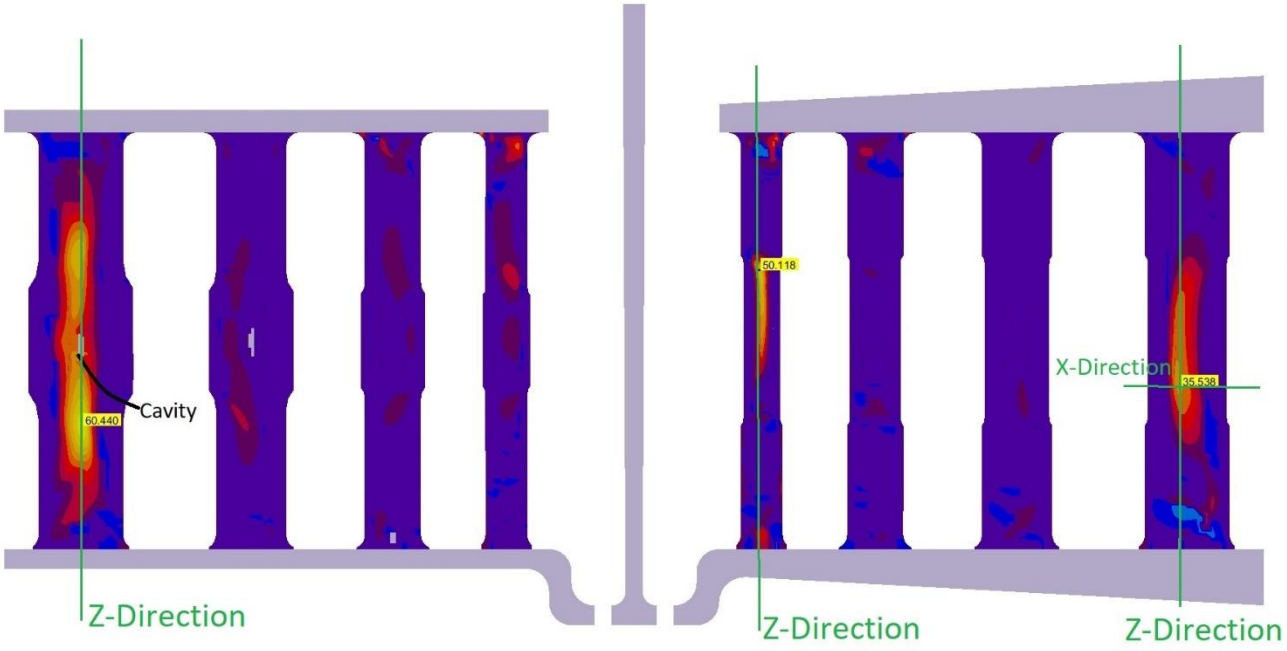

Figure 21: Measurement lines indicated in the x and z-direction at which the results between MAGMASOFT® and neutron diffraction will be compared

The simulation results were also shown, as part of the “neutron diffraction residual stress results” (for comparison between the simulated and experimental results), in the form of graphs along the lines presented in Figure 21, see section 5.2 – 5.5.

4. VERIFICATION

4.1 Casting

4.1.1 General

Three identical trees were cast using ductile cast iron to replicate the simulated castings as discussed in section 3.1. Three branches, A, B and C (Figure 19), with the highest simulated residual stress values were cut from two of the trees. The branches were cut from the trees using a band saw (rather than using a grinding machine) so that too much heat was not generated, thus ensuring that no unnecessary machining related residual stress was induced. The third cast tree was used for reference purposes.

4.1.2 Moulds

Expandable moulds were made from Furan resin silica sand (discussed in section 3.1) using the mould box (see Figure 22). Three trees (with the form shown in Figure 11) were cast using EN-GJS-400 ductile cast iron at High Duty Castings (Pty) Ltd., situated in Boksburg, South Africa.

Table 8: GJS-400 ductile cast iron properties and composition (Anon, 2009; Anon, 2014)

EN-GJS-400 cast iron material			
Properties		Element	Weight %
Tensile strength (min) MPa	400	C (Carbon)	2.5 - 3.8
Yield strength (min) MPa	250	Si (Silicon)	0.5 - 2.5
Elongation (min) %	1500%	Mn (Manganese)	0.2 - 0.5
Density g/cm^3	7.3	P (Phosphorous)	≤ 0.08
Brinell Hardness	130-180	S (Sulphur)	≤ 0.02

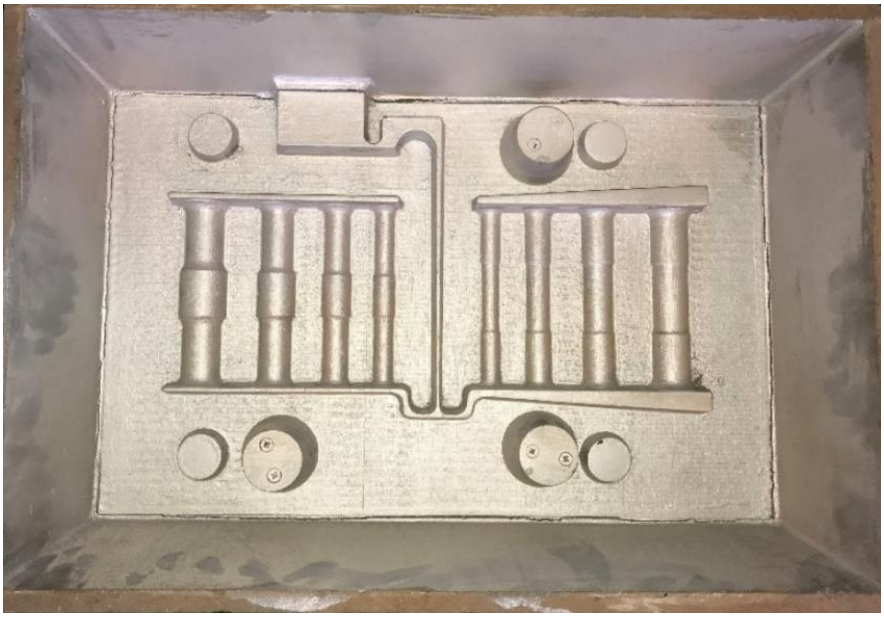

Figure 22: Mould box which was used to make the sand moulds in

During the casting process, the two halves of the mould were not aligned correctly in the horizontal direction; thus, causing the casting to have an offset in the middle as shown in Figure 23.

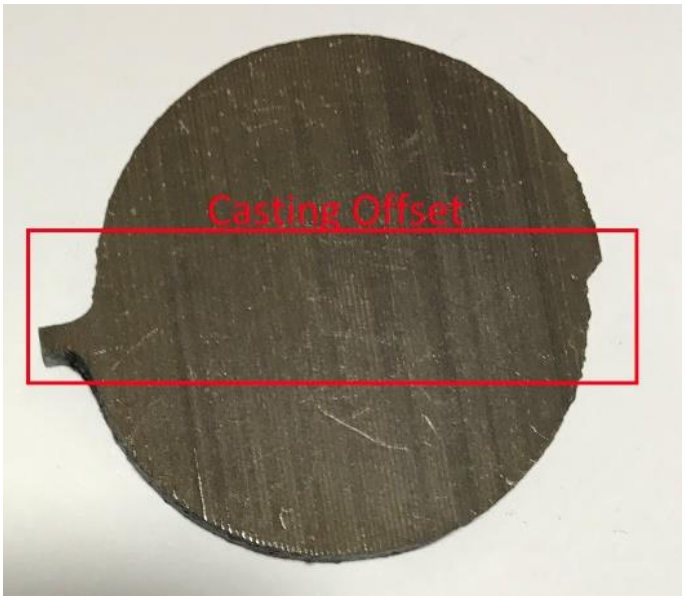

Figure 23: Casting offset on cast branches – cut out of branch 1 from tree 3

Due to the castings that were cast with an offset, locating a reference point for the residual strain measurements were complicated. This caused that the locations measured by means of neutron diffraction were not accurate to those extracted from the simulations. Thus, the residual strain measurements had to be taken at as close as possible proximity to the middle of the samples in order to compare the results to those of the simulation results.

4.2 X-ray Tomography

Due to the prediction of cavities in the branches as discussed in section 3.3, it had to be verified for the sake of the neutron diffraction strain measurements. If the simulation was accurate and cavities were present in the casting, the position and size thereof had to be known. The reason for this is that corrections for spurious strains must be made in terms of the neutron diffraction data and measurements where the cavities are present. Thus, if corrections were not made, it could have impacted the measurement results negatively.

The cavities were verified on sample Tree1Branch1(V2) – see Figure 26, as this was the branch predicted by MAGMASOFT® to have the largest cavity present as supported by section 3.3. X-ray Tomography at Necsa's facilities were used for these measurements (Hoffman & DeBeer, 2012).

In Figure 24, three X-ray images can be seen of the bottom, middle and upper section of sample T1B1(V2), respectively.

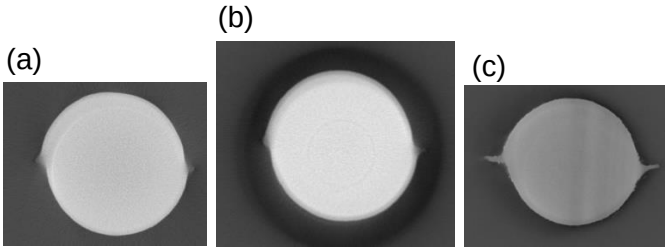

Figure 24: (a) Bottom, (b) middle and (c) upper section views of the X-ray Tomography on sample T1B1(V2)

The X-ray Tomography results were converted from a .stl file (consisting of numerous X-ray images similar to those in Figure 24) to a solid. This was done by importing the .stl file into FreeCAD (an open-source parametric 3D modeler) and simplifying the mesh due to the mesh being too complicated for Solidworks to convert it directly into a solid. The simplified mesh was then reconstructed and repaired using MeshLab (an open source system for processing and editing 3D triangular meshes) and then exported as a new and simplified .stl file. The new .stl file was then converted into a solid, using Solidworks. In Figure 25, the solid is shown as cut in half.

Figure 25: (a) Top and (b) front cut view of the reconstructed solid obtained by means of X-ray tomography

It was established that there were no cavities present in the cast sample T1B1(V2), after the X-ray Tomography model reconstruction (as shown in Figure 25). The neutron diffraction measurements could, therefore, be performed without correcting for spurious strains due to cavities. Since there were no cavities found in the sample that was predicted to have the biggest cavity by MAGMASOFT®, it was assumed that the other samples also had no cavities.

When considering the cavities, and the reason why they were predicted in MAGMASOFT®, and were verified not to be present by means of the X-ray Tomography, may be due to the following reasons:

- The fact that the mould was not clamped and sealed correctly and the liquid metal formed a large flash (as seen in Figure 23 and Figure 28) – also a result of the casting offset as discussed in section 4.1.2. This flash caused the usage of excess metal and the liquid metal could flow through the mould without forming a cavity.
- The actual casting process did not flow and cool down as simulated in the MAGMASOFT® simulation.

4.3 Neutron Diffraction

4.3.1 General

The residual strains in the branches were measured using the MPISI neutron diffraction instrument at the South African Nuclear Energy Corporation (Necsa) SOC Limited. The branches from the duplicated trees (mentioned in section 4.1.1) were then respectively heat-treated and machined, as discussed in section 3.1. A similar neutron diffraction analysis was then carried out on them to determine the residual stress.

The residual stress values converted from the neutron diffraction residual strain analysis were compared with the simulated values and the results discussed with relevance to casting optimisation.

The residual strains in the branches were obtained using Equation 29 by means of comparing the reference d-spacing value of the material (d_0) to the d-spacings (d) measured in the material using the MPISI neutron diffraction instrument at Necsa under the supervision of Dr Deon Marais.

The trees and branches were numbered as illustrated in Figure 26.

Figure 26: Tree and branch numbering

Branch numbering was done as follows: Tree(x)Branch(x), thus in short T(x)B(x), with “x” the unknown in this case.

It was decided that the castings would be measured as follows (see Figure 21):

- Casting T1B1(V2) – along the z-direction of the x-, y- and z-component stresses;
- Casting T1B3(V2) - along the x- and z-direction of the z-component stresses; and
- Remaining branches - only at the chosen points along the z-direction of the z-component stresses, which is at the point of maximum residual stress indicated by MAGMASOFT®.

The reason for investigating T1B1(V2) in depth, was due to the fact that it was the branch that MAGMASOFT® predicted to have the most residual stress present. The reason for the comparison of only the z-component stresses in the remaining branches, was because of the fact that x- and y-component stresses were minor as predicted by MAGMASOFT® (discussed in section 3.3).

4.3.2 Heat Treated Branches

The branches that were heat treated were those from tree 1, thus branch T1B1(V3), T1B2(V3) and T1B3(V3). It is important to note that this process was undertaken only after the first residual stress measurements on the branches, T1B1(V2), T1B2(V2) and T1B3(V2).

This process was undertaken due to the following reasons:

- To determine whether the residual stress within the sample decreases by using the correct heat treatment cycle for stress relieving;
- To determine whether MAGMASOFT® correctly predicts a relief in stress; and
- To verify the stress relief heat treatment cycle as per section 2.8.

The heat treatment process was carried out in a high temperature oven at the North-West University’s Mechanical Engineering Department. The heat treatment cycle is presented in Table 3.

4.3.3 Machined Branches

The samples that were machined were those from tree 2, thus sample T2B1(V4), T2B2(V4) and T2B3(V4). It is important to note that this process was undertaken only after the first residual stress measurements on the branches T2B1(V2), T2B2(V2) and T2B3(V2).

This process was undertaken due to the following reasons:

- To determine whether the residual stress within the samples increase or decrease by machining the samples; and
- To determine whether MAGMASOFT® correctly predicts an increase or decrease in stress.

The sample branches were machined at the North-West University's Mechanical Engineering Department to uniform samples (see Figure 27) of the same diameter; a detailed drawing of the machined samples can be viewed in Appendix A.

Figure 27: Machined uniform tensile test samples, samples shown are T2B1(V4), T2B2(V4) and T2B3(V4)

4.3.4 Neutron Diffraction Measurements

The MPISI neutron diffraction instrument makes use of software called ScanManipulator to process the data. ScanManipulator applies function fitting and corrections automatically, to existing data files or on real time data gained directly from the neutron detector's software (Marais, 2016:202).

Before the neutron diffraction residual stress measurements could be conducted on the branches, a reference d-spacing value (d_0) was required supported by Equation 29. The reference d-spacing value (d_0) was obtained using the following different methods:

1. By means of measuring (using neutron diffraction), a sample cut from a section in the casting – noted as d_0^1.

   The samples, (5 x 5 x 5) mm in size, were cut from different sections in the third cast tree (as mentioned in section 4.4.1) by using a wire electrical discharge machine (EDM). The wire EDM makes use of a fine wire and constant water cooling to cut material. This ensures that the material being cut is not subjected to high heat due to

friction. Thus, by using this method, unnecessary stresses in the samples were not induced. The sections where the samples were cut from, were two different positions in branch 1 and one position in the outlet of the pouring basin where MAGMASOFT® indicated different stress values (Figure 28).

2. By using the average d -spacing values measured of each branch, as the d_0 values – noted as d_0^2.

   This method was a viable alternative due to the reason that the increments at which the neutron diffraction measurements were taken, were evenly spaced. Another reason (discussed in section 2.3) for this is that the residual stress balance in terms of positive and negative stress over the sample should equal 0; thus, the residual stress remains in equilibrium.

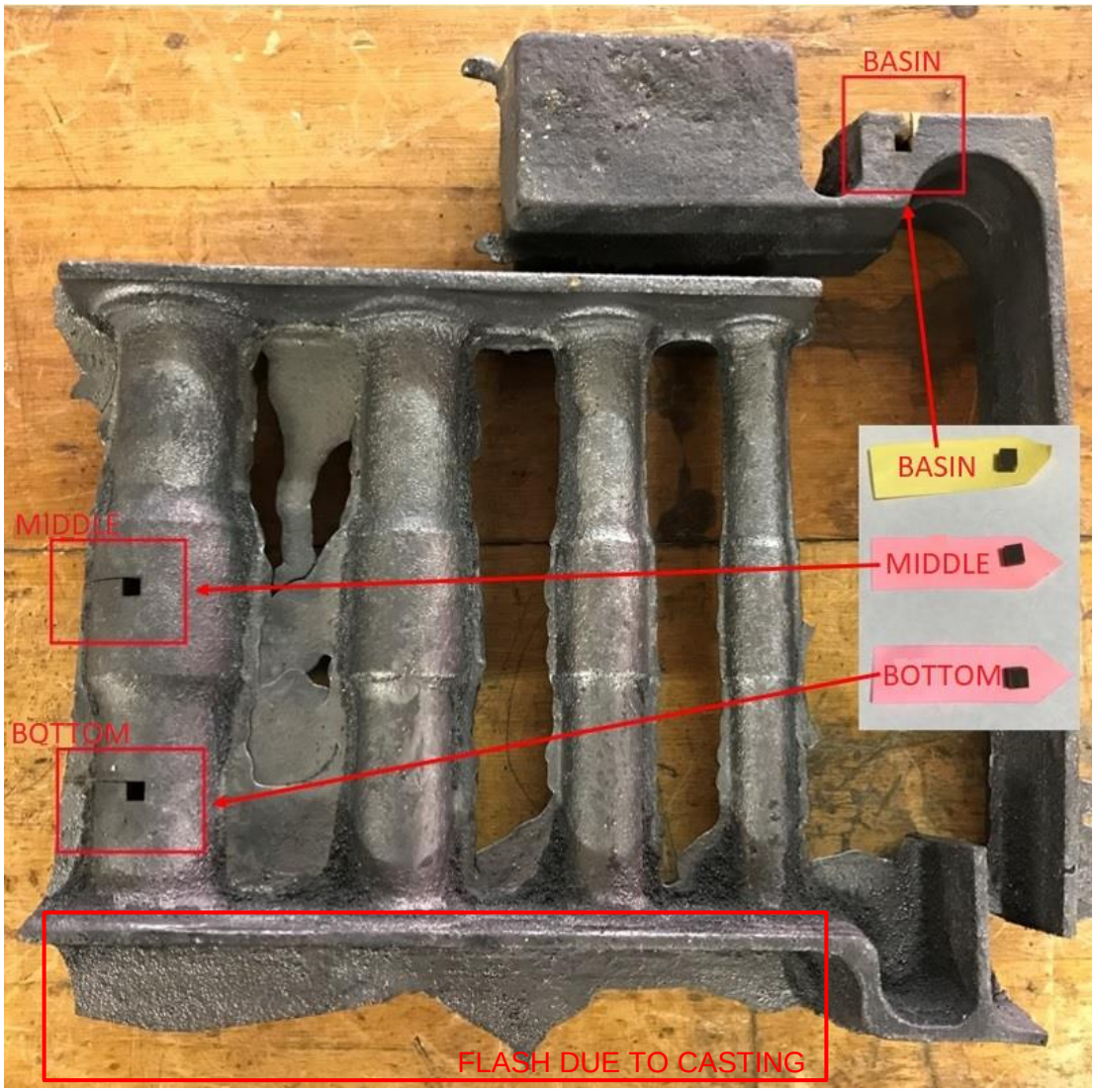

Figure 28: Tree 3 from which the reference samples were cut – illustrating the positions

The outcomes and results of the two methods are shown in section 5.1 and discussed in section 6.1.

Diffraction peak parameters namely peak intensity, integrated intensity, peak centre, background, full-width-half maximum, among others have related uncertainties. These diffraction peak parameters had to be determined from the data obtained by neutron diffraction by means of fitting the Gaussian function to the corrected peak data using a least-squares method. The uncertainties mentioned were shown by means of error bars in the residual stress result graphs in section 5.2 – 5.5 (Marais, 2016:201).

The strain measurement on the branches consisted of measuring the orientation and depth dependence of a pre-selected diffraction peak – in this case the Fe(211) peak. The peak angle was determined by neutron diffraction, in this case a 2Θ value of 90° (resulting in a cubic gauge volume), by means of a Gaussian function fitting and then converted to d-spacing. The slit positioning on the instrument was 55 mm from the centre of rotation and the measurement times per position is summarised in Table 9 for these measurements, with a wave length of 1.67 Å and a gauge volume size of 2 x 2 x 2 mm. The samples were aligned using a laser alignment system at the MPISI instrument.

Table 9: Neutron Diffraction Boundary Conditions Summary

Neutron Diffraction Measurement Boundary Conditions		
Gauge volume	2 x 2 x 2 [mm]	
Slit positioning from centre of rotation	55 [mm]	
Wavelength	1.67 [Å]	
Diffraction peak measured	Fe(211)	
2Θ value	90 [°]	
Measurement time per position	T1B1 (V2)	1200 [sec]
	T1B2 (V2)	2500 [sec]
	T1B3 (V2)	3600 [sec]
	T2B3 (V2)	3600 [sec]
	T1B1 (V3)	3600 [sec]
	T1B2 (V3)	720 [sec]
	T1B3 (V3)	3600 [sec]
	T2B1 (V4)	120 [sec]
	T2B2 (V4)	126 [sec]
	T2B3 (V4)	127 [sec]

The d-spacing values (d) were then inserted into Equation 29 together with the unstressed reference d-spacing values (d_0) to determine the strains at the different positions in the branches. The results of automatic function fitting of numerous datasets were exported to

Microsoft Excel by ScanManipulator. Further calculations were then conducted (Marais, 2016:202).

The residual strains then had to be converted to residual stress as per Equation 31 - Equation 33, to be compared with the results obtained from the MAGMASOFT® simulation of section 3.

5. NEUTRON DIFFRACTION RESIDUAL STRESS RESULTS

The numerical residual stress results of section 5.2 – 5.5 is presented in Appendix B. The neutron diffraction residual stress results for every simulation conducted, is shown in the form of graphs in section 5.2 – 5.5. The graphs were set up as representation of the numerical results consisting of the residual stresses, converted from the neutron diffraction strain measurements, over position.

The stress values were extracted from the z-direction stress components along the z-axis (except for sample T1B1(V2) as mentioned in section 4.3.1) (vertical axis) direction (Figure 21) as this was where MAGMASOFT® predicted the highest order of residual stress. The residual strain measurements by means of neutron diffraction were obtained at 30 coordinates, in comparison to 100 coordinates MAGMASOFT® used, along the measurement line in z-axis direction.

Due to the difference in the amount of data points, a 6^{th} order polynomial trend line was fitted to the data. This was done to even out the results obtained from the neutron diffraction measurements to be able to make a better comparison between the MAGMASOFT® and neutron diffraction results. Note that the positive value results shown on the graphs are tensile residual stresses, and negative value results are compressive residual stresses.

The MAGMASOFT® residual stress simulation results obtained from section 3.2, are plotted on the graphs for comparative reasons as mentioned in section 3.3.

5.1 Measurements of the d-spacing (d_0) values

The d_0 values were obtained as per section 4.3.4 and is presented in Table 10.

Table 10: Resulting d_0 values obtained using the two different methods

Cut sample d_0 values - d_0^1		Average d-spacing value used as d_0 values - d_0^2	
Position	**Value (Å)**	**Sample**	**Value (Å)**
BASIN	1.1801	T1B1 (V2)	1.1799
MIDDLE	1.1801	T1B2 (V2)	1.1799
BOTTOM	1.1800	T1B3 (V2)	1.1799
		T2B3 (V2)	1.1800
		T1B1 (V3)	1.1799
		T1B2 (V3)	1.1799
		T1B3 (V3)	1.1799
		T2B1 (V4)	1.1799
		T2B2 (V4)	1.1799
Average	1.1801	T2B3 (V4)	1.1799

5.2 Tree 1 - Sample T1B1(V2), T1B2(V2) and T1B3(V2) without Runners

5.2.1 T1B1(V2)

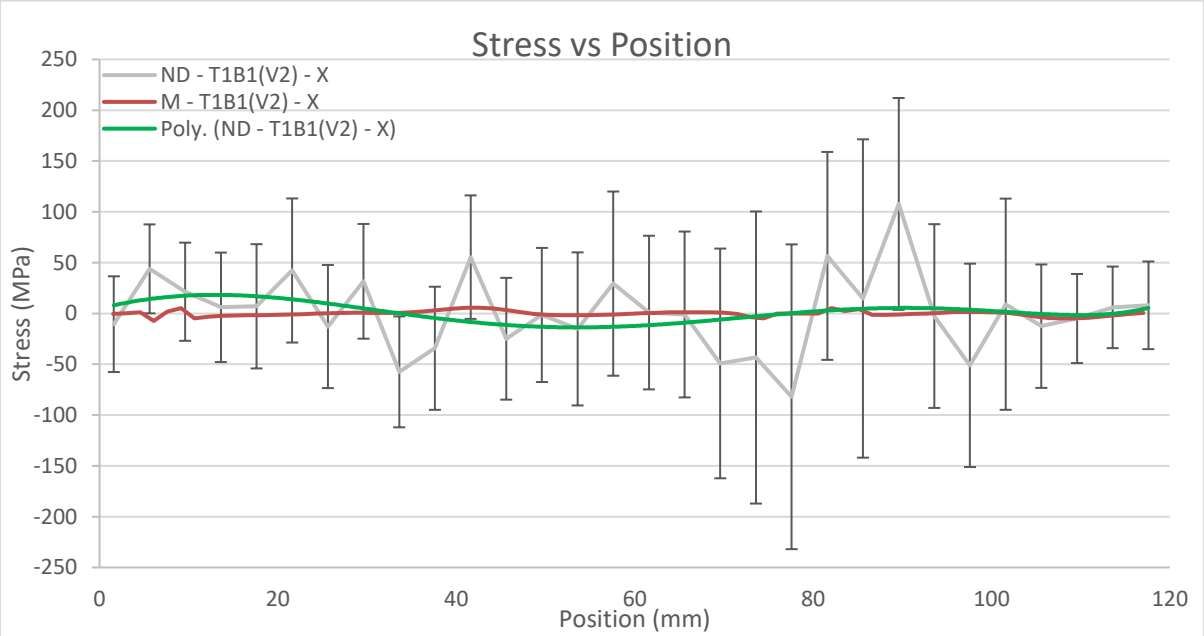

Figure 29: T1B1(V2) – MAGMASOFT® vs neutron diffraction result in the z-direction of the x-direction stress component

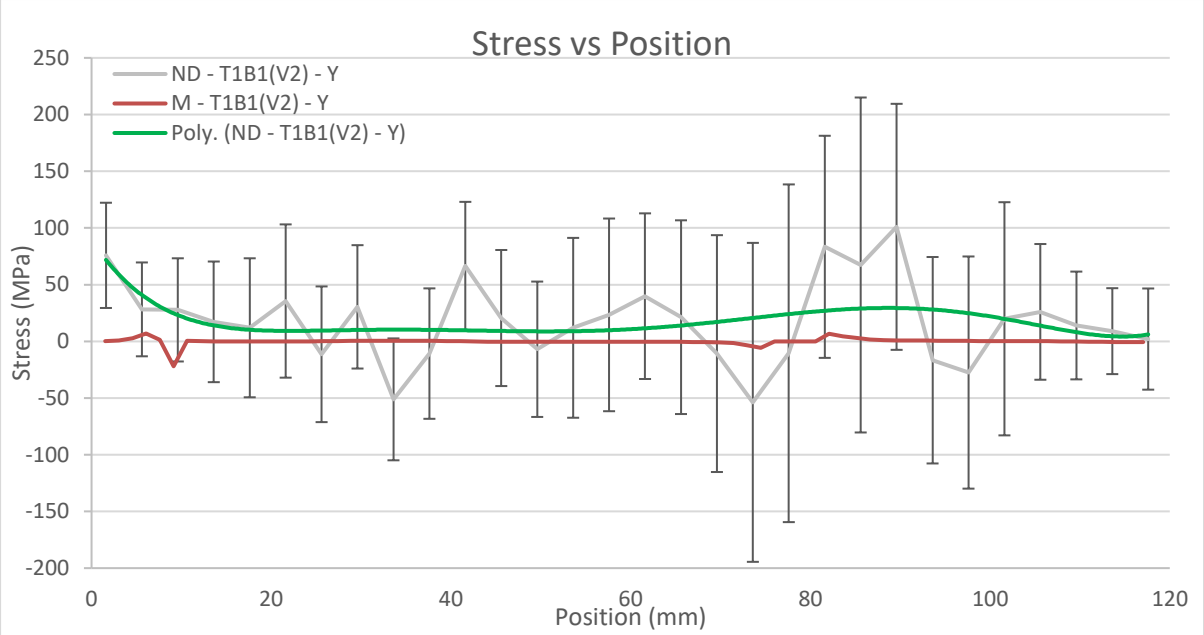

Figure 30: T1B1(V2) - MAGMASOFT® vs neutron diffraction result in the z-direction of the y-direction stress component

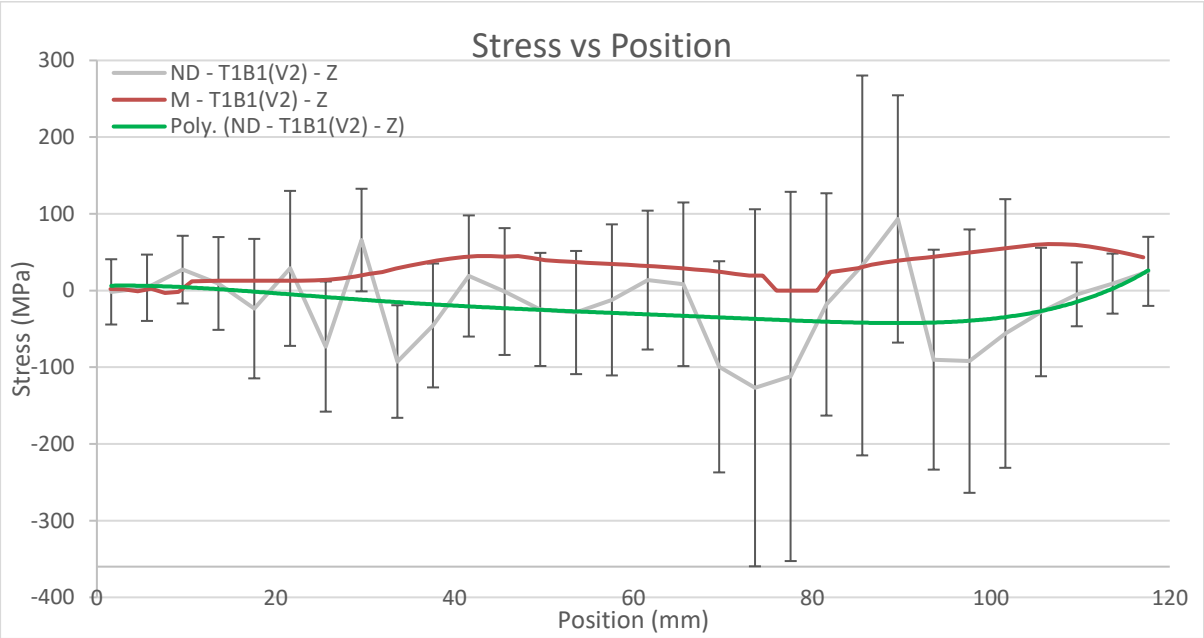

Figure 31: T1B1(V2) - MAGMASOFT® vs neutron diffraction result in the z-direction of the z-direction stress component

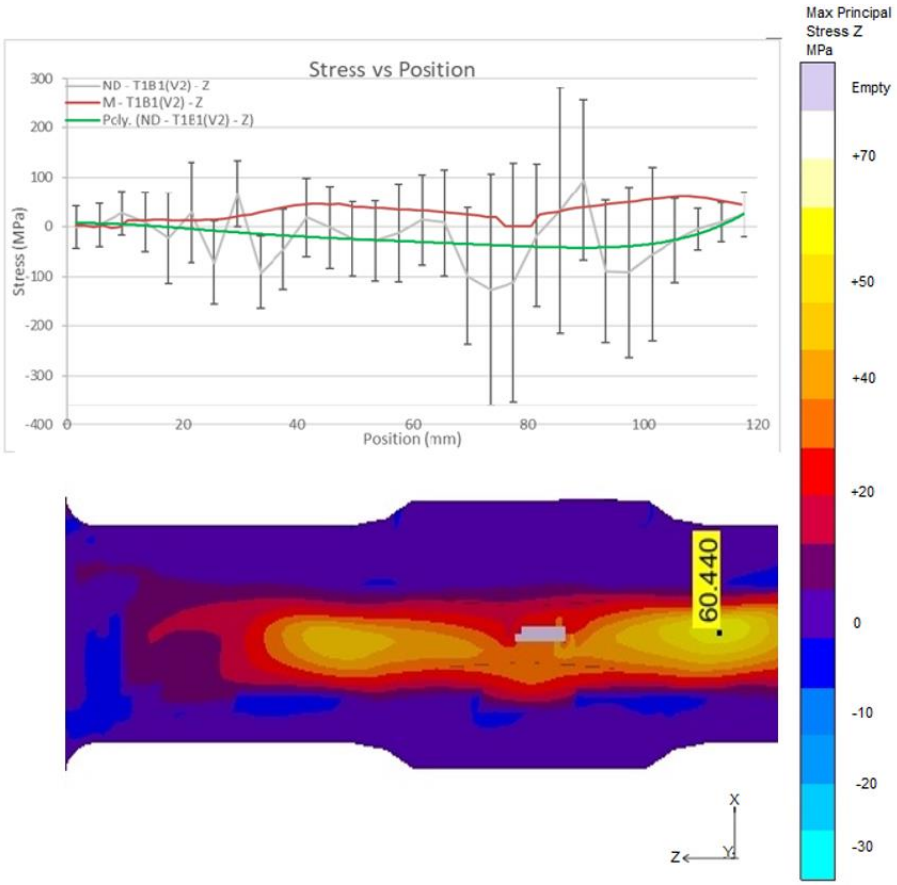

Figure 32: T1B1(V2) – Direct schematic comparison of the MAGMASOFT® vs neutron diffraction result in the z-direction of the z-direction stress component

5.2.2 T1B2(V2)

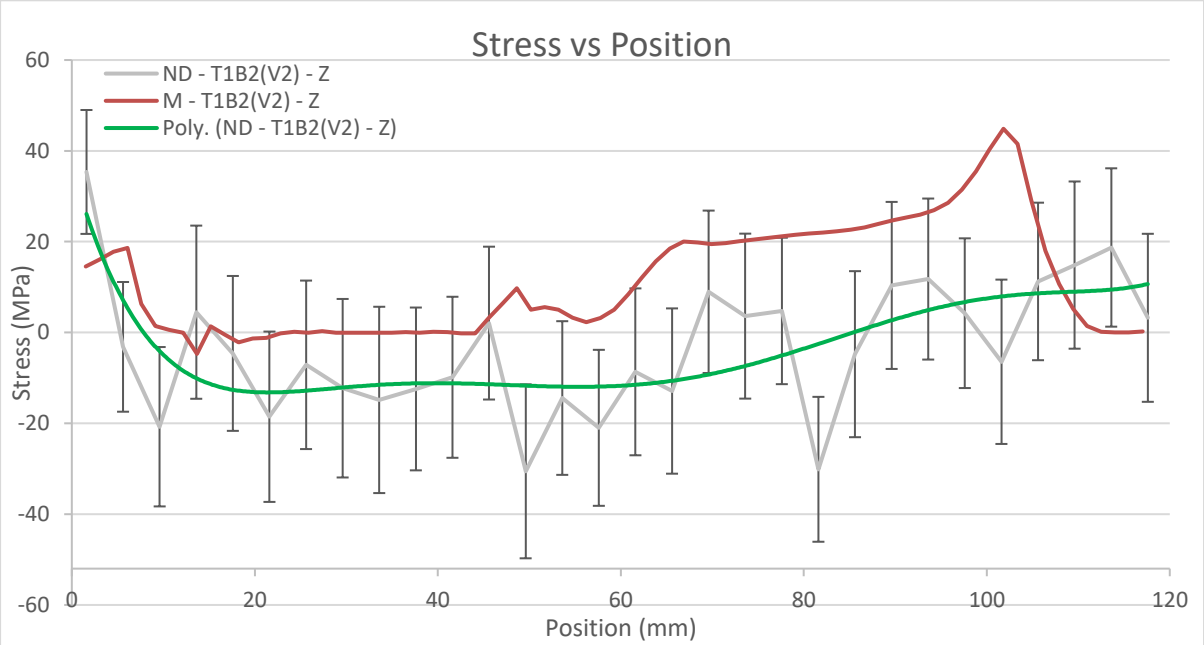

Figure 33: T1B2(V2) - MAGMASOFT® vs neutron diffraction result in the z-direction of the z-direction stress component

5.2.3 T1B3(V2)

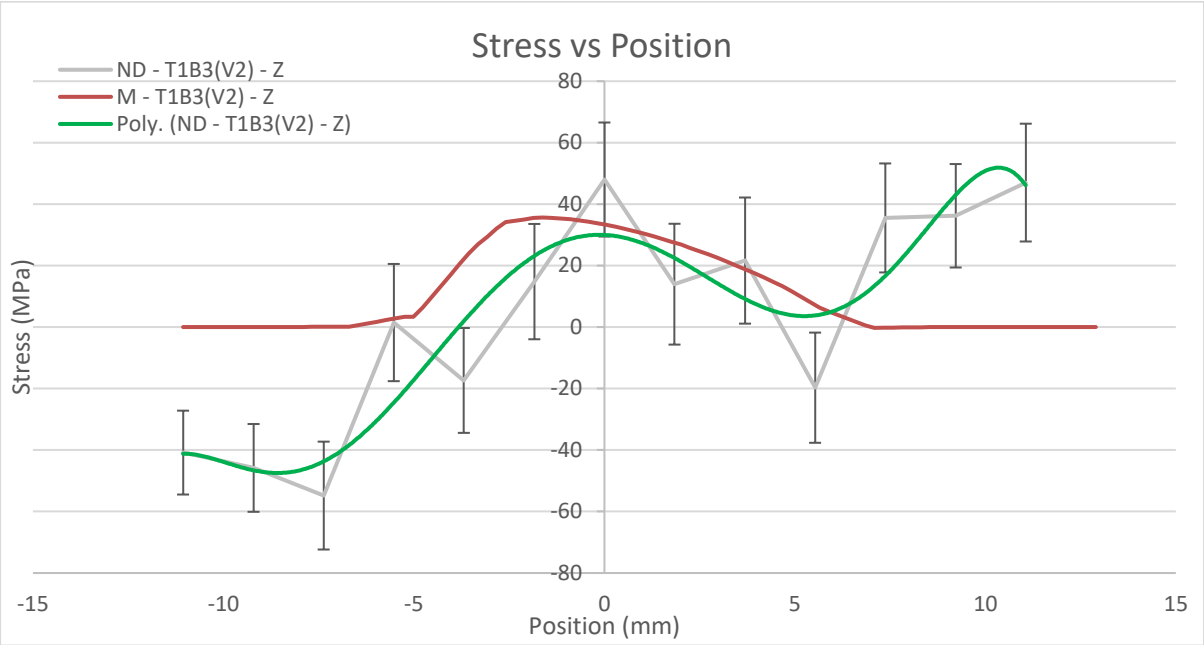

Figure 34: T1B3(V2) - MAGMASOFT® vs neutron diffraction result in the x-direction of the z-direction stress component

Figure 35: T1B3(V2) - MAGMASOFT® vs neutron diffraction result in the z-direction of the z-direction stress component

5.3 Tree 2 - T2B3(V2) without Runners

The MAGMASOFT® results of this Tree is the same as those from Tree 1, as all the simulation conditions are the same.

It was assumed that the casting conditions were identical between Tree 1 and Tree 2 and, subsequently, this meant that the results between Tree 1 and Tree 2, should have been the same.

It was chosen to only measure sample T2B3(V2) using neutron diffraction. This was done only for comparative purposes.

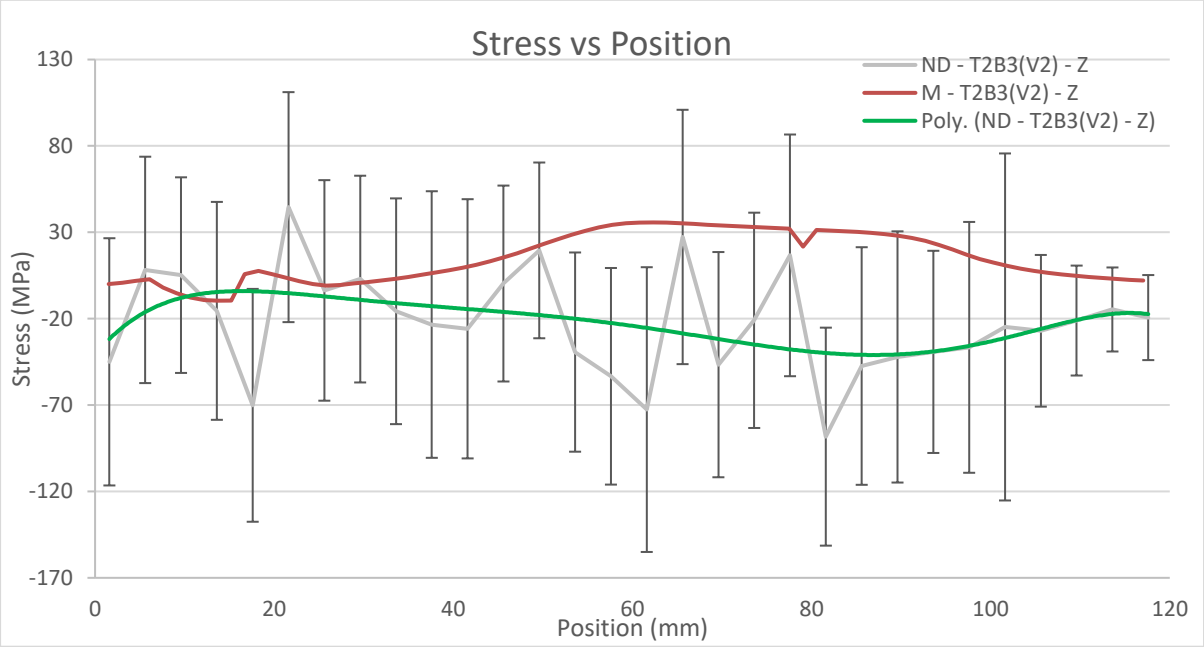

Figure 36: T2B3(V2) - MAGMASOFT® vs neutron diffraction result in the z-direction of the z-direction stress component

5.4 Tree 1 – T1B1(V3), T1B2(V3) and T1B3(V3) Heat Treated

5.4.1 T1B1(V3) Heat Treated

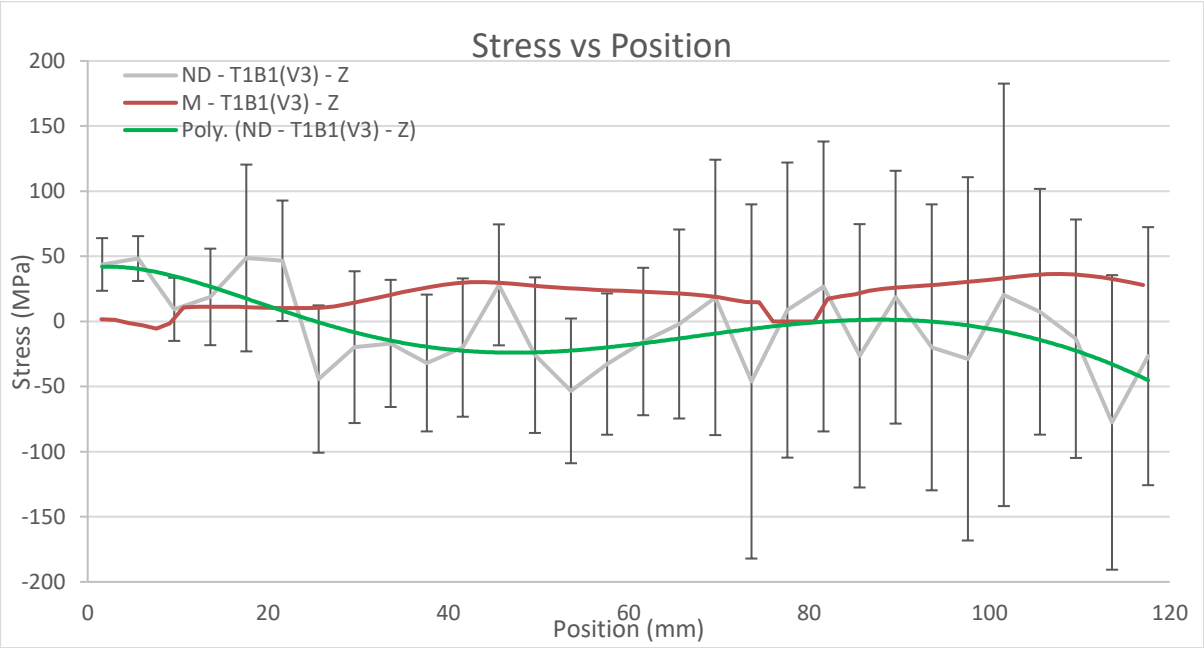

Figure 37: T1B1(V3) Heat Treated - MAGMASOFT® vs neutron diffraction result in the z-direction of the z-direction stress component

5.4.2 T1B2(V3) Heat Treated

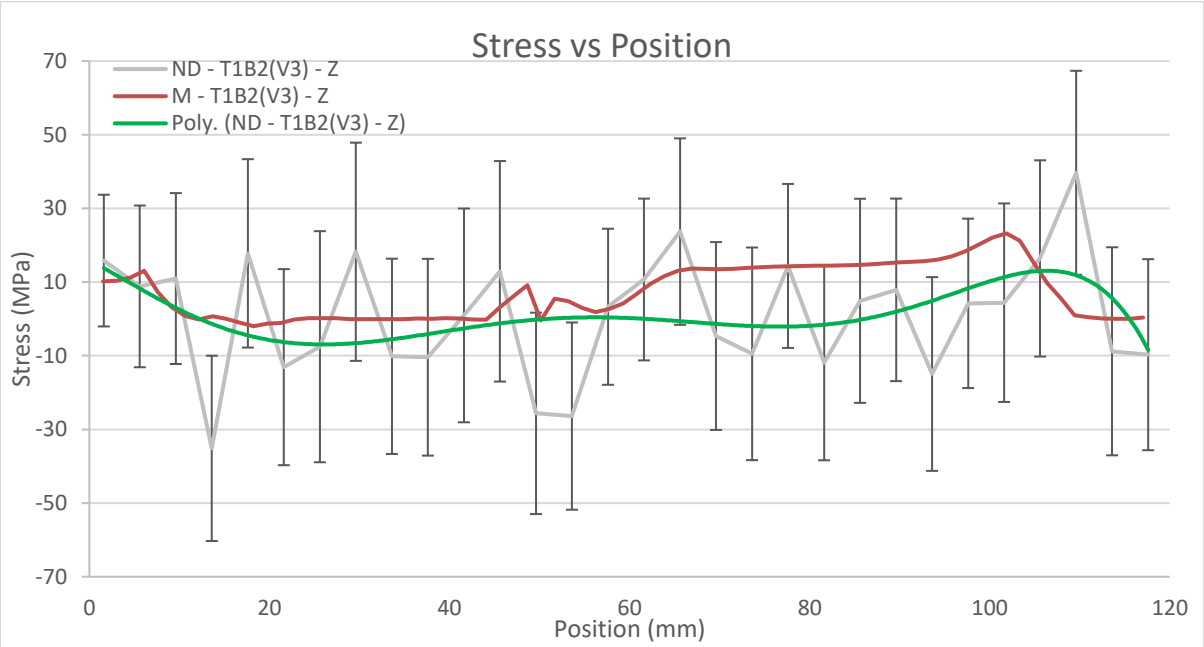

Figure 38: T1B2(V3) HT - MAGMASOFT® vs neutron diffraction result in the z-direction of the z-direction stress component

5.4.3 T1B3(V3) Heat Treated

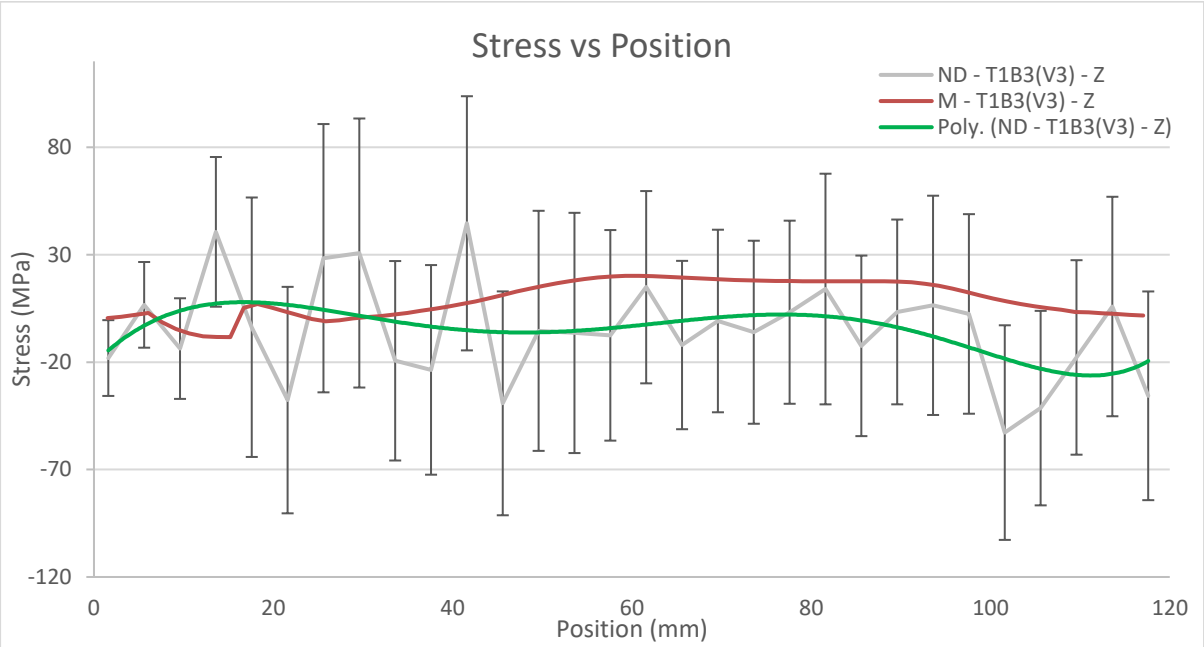

Figure 39: T1B3(V3) Heat Treated - MAGMASOFT® vs neutron diffraction result in the z-direction of the z-direction stress component

5.5 Tree 2 – T2B1(V4), T2B2(V4) and T2B3(V4) Machined

5.5.1 T2B1(V4) Machined

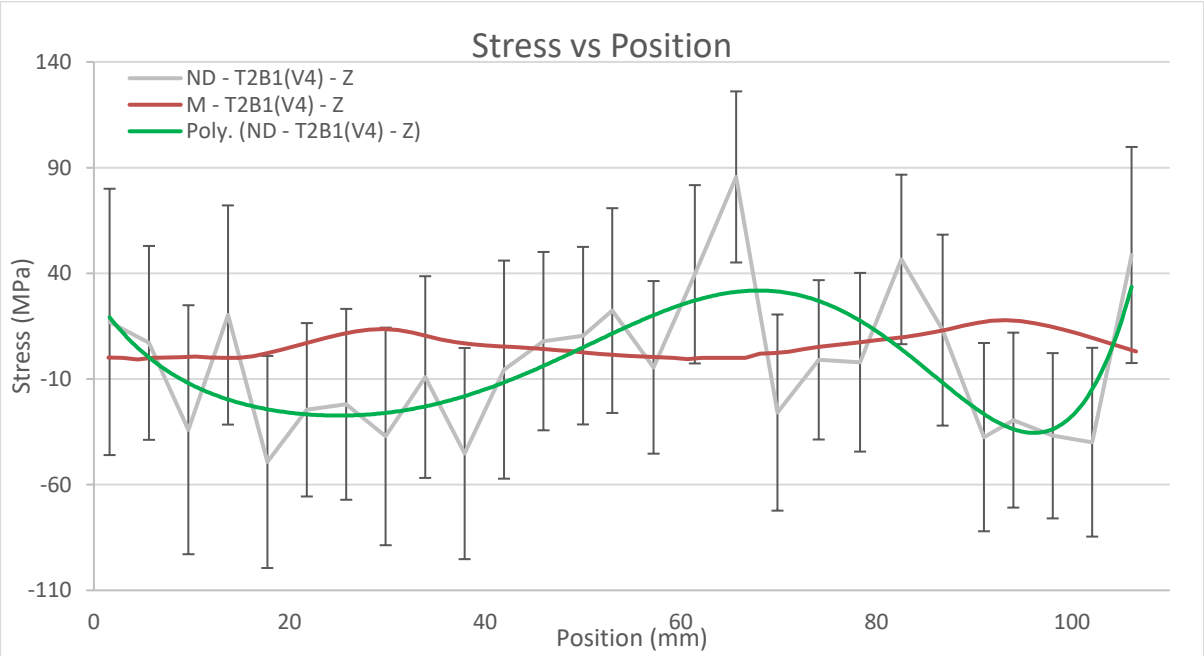

Figure 40: T2B1(V4) Machined - MAGMASOFT® vs neutron diffraction result in the z-direction of the y-direction stress component

5.5.2 T2B2(V4) Machined

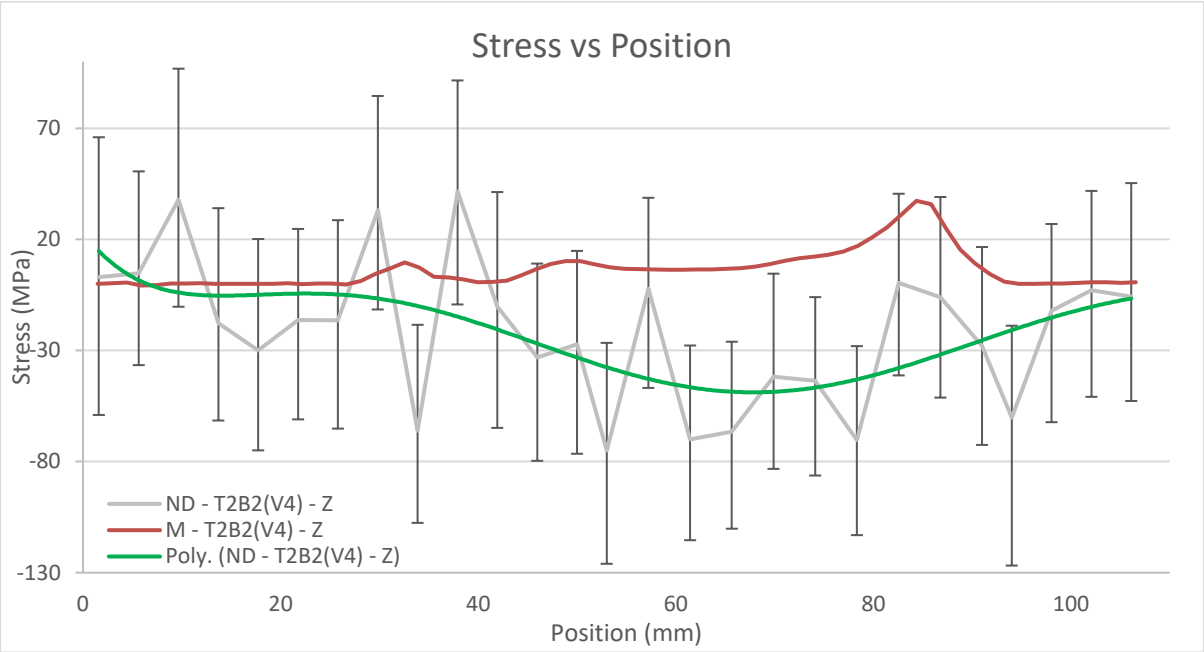

Figure 41: T2B2(V4) Machined - MAGMASOFT® vs neutron diffraction result in the z-direction of the z-direction stress component

5.5.3 T2B3(V4) Machined

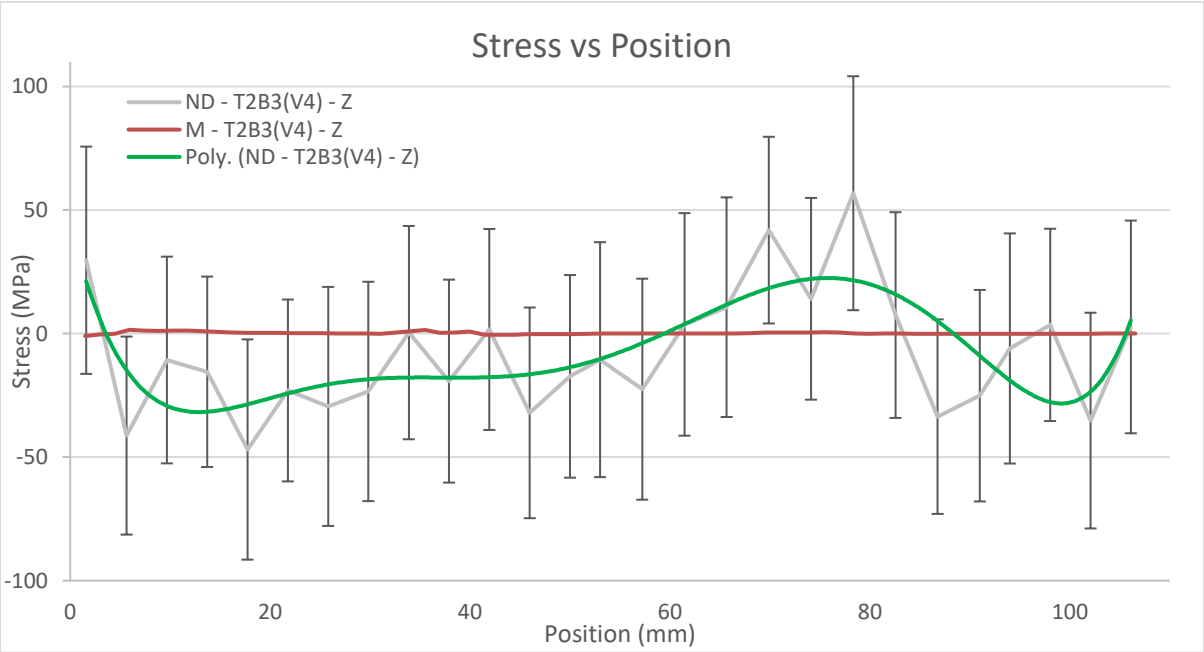

Figure 42: T2B3(V4) Machined - MAGMASOFT® vs neutron diffraction result in the z-direction of the z-direction stress component

6. DISCUSSION

6.1 Measurement Results of the Reference d-spacing (d_0) Values

In Table 10 (section 5.1), the reference d-spacing values between the different methods shown, is evident to differ very little. By interpreting Equation 29, which calculates the strain using the d and d_0 values, it is evident that a slight change in the d_0 values, causes a big change in the calculated strain values which then directly influences the residual stress results.

The two methods (discussed in section 4.3.4) were investigated and method 1 was found to be unphysical for the reason that by using the cut samples d_0 values (noted as d_0^1) the results only gave negative residual stresses.

It was found that, when investigating the residual stress results calculated using the average d_0 values (noted as d_0^2), the results seemed to be much more logical and comparative to those of the MAGMASOFT® simulation.

The reason why method 1 was unphysical could be due to numerous reasons including the following:

- The tree from which the cut samples were cut could have been cast from a material with a slightly different composition;
- The wire EDM cutting could have had a slight influence on residual stress in the cut samples noted as d_0^1; and
- The casting conditions between the different trees could have been slightly different.

From the above it was decided to use the average d_0 values obtained from method 2 for the experimental results, thus noted as d_0^2.

6.2 Residual Stress Results

6.2.1 General

A in depth investigation was done on sample T1B1(V2) (mentioned in section 4.3.1) due to the fact that it was the sample predicted to have the highest residual stress. The investigation was done on the xz-plane of the z-component stresses; thus, a full residual stress map of this plane was measured. The neutron diffraction residual stress map was set up using MATLAB

(a multi-paradigm numerical computing environment) by inserting the results into a 2D plot with a colour legend.

The residual stress map of the results, between the simulated and experimental results in this plane, is presented in Figure 43 below.

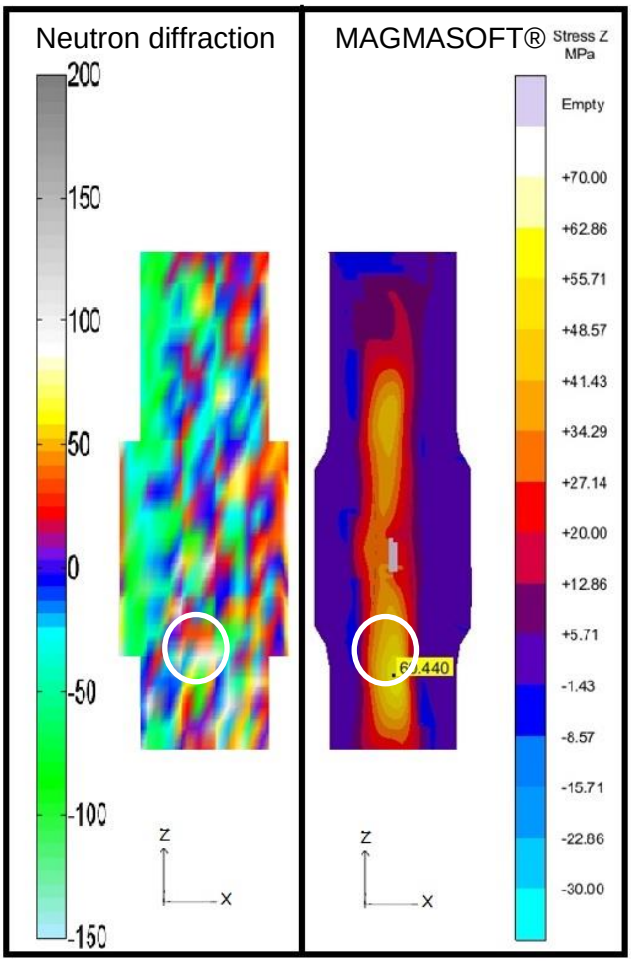

Figure 43: T1B1(V2) - MAGMASOFT® vs neutron diffraction result in the xz-plain of the z-direction stress component

The full residual stress map results by means of neutron diffraction vs MAGMASOFT® presented in Figure 43, show maximum residual stress in a corresponding area of about 60 MPa (indicated on Figure 43), the remaining results do not compare satisfactorily.

Although the MAGMASOFT® and neutron diffraction residual stress results do not match very accurately, the following is decided from the results:

- It is evident from MAGMASOFT® and neutron diffraction measurements that the x- and y-direction residual stress components are very low and can be ignored (Figure 14 and Figure 15). Therefore, only the z-component residual stress results were further shown and discussed.

- The z-directions stress components were higher and is supported by the results from both MAGMASOFT® and the neutron diffraction measurements (Figure 16, Figure 31 and Figure 32).

- It is also evident that MAGMASOFT® and the neutron diffraction measurements both show evidence that Sample T1B1(V2) has the highest order of residual stresses when observing Figure 29 - Figure 42.

When considering sample T1B3(V2) and T2B3(V2), (see section 5.3 and Figure 44), the results do not match very accurately. These results were supposed to correspond, as they are the exact same samples, just from the other tree. This shows more evidence that there may have been different casting conditions or slight material composition differences between the different cast trees (in this case between Tree 1 and Tree 2).

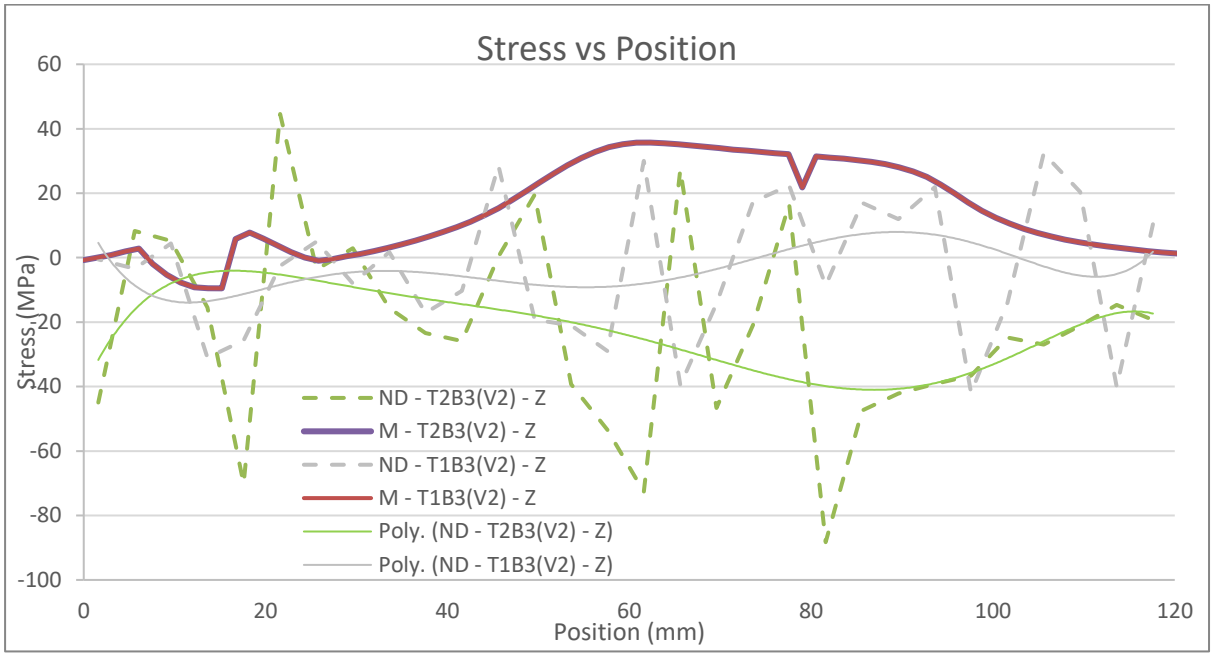

Figure 44: T1B3(V2) vs T2B3(V2) - MAGMASOFT® vs neutron diffraction result in the z-direction of the z-direction stress component

With the data obtained (Figure 29 - Figure 42), trends between MAGMASOFT® and the neutron diffraction results are apparent (between 10 – 80 mm in position). Even though the values do not match very well, most of the values fall within the experimental error limit (as per the error bars on the graphs).

When analysing the data (Figure 29 - Figure 42), peaks can be observed in the neutron diffraction measurement results (the data has a zig-zag trend), whereas the MAGMASOFT® results have even curves. This is due to the neutron diffraction measurements not having as

much data points (measurement increments, also discussed in section 5) as the MAGMASOFT® simulation results. Furthermore, it is important to note that the amount of increments used for the neutron diffraction measurements were not in the author's control. The added 6th order polynomial line fitted to the neutron diffraction residual stress results made the data much more comparable.

It is evident, by the results of sample T1B1(V2) and T1B1(V3) (see Figure 31 and Figure 37), that between 75 – 85 mm in position a section of 0 residual stress can be observed in the MAGMASOFT® results. This is due to the cavity MAGMASOFT® predicted discussed in section 4.2.

It is also observed that in these samples (see Figure 29 - Figure 31 and Figure 37), the error bars enlarge between about 70 - 110 mm in position. These enlarged error bars are due to the thicker diameter section in sample T1B1. The neutrons had to penetrate deeper within the branch, increasing the path-length and thereby, reducing the intensity of the diffracted beam.

6.2.2 Heat Treated and Machined Branches

It is evident from the results (see section 5.4 and Figure 37 - Figure 39) that, by applying the correct heat treatment to the samples, the residual stresses do, in fact, decrease. By comparing the MAGMASOFT® and the neutron diffraction measurement results, it is evident that the values do not compare accurately, although both show a decrease of the residual stresses within the components. This supports the literature from section 2.8.

In Figure 45 below, sample T1B1(V2) was compared with the heat-treated sample T1B1(V3), since T1B1(V2) showed the most residual stress as mentioned in section 4.3.1.

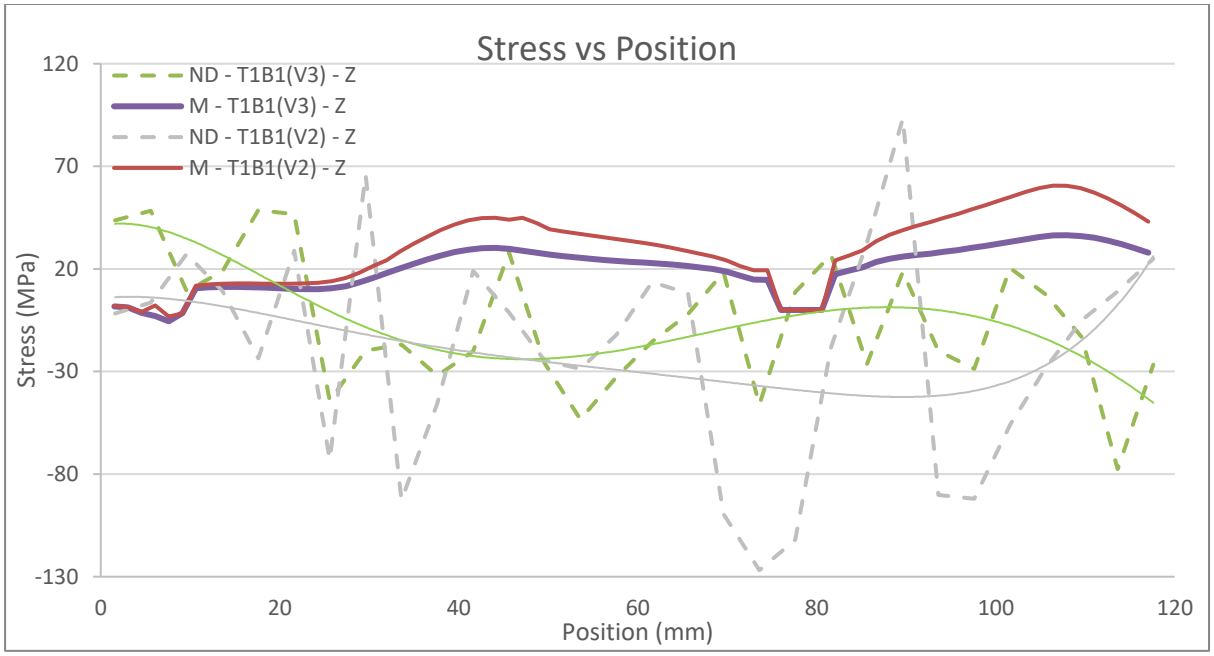

Figure 45: T1B1(V2) vs T1B1(V3) heat treated - MAGMASOFT® vs neutron diffraction result in the z-direction of the z-direction stress component

According to these results, it can be assumed that, if the heat treatment is applied for a longer period, the residual stress might decrease more.

When considering the machined sample results (see section 5.5 and Figure 40 - Figure 42), it is evident, in this case, that machining causes a decrease in the residual stresses within the components. By comparing the MAGMASOFT® and the neutron diffraction measurement results (Figure 46), it is evident that the values do not compare accurately, although both show a decrease in the residual stress within the components.

In Figure 46, sample T2B3(V2) was compared with sample T2B3(V4), because T2B3(V2) was the only sample from Tree 2 to be measured by means of neutron diffraction, as mentioned in section 5.3.

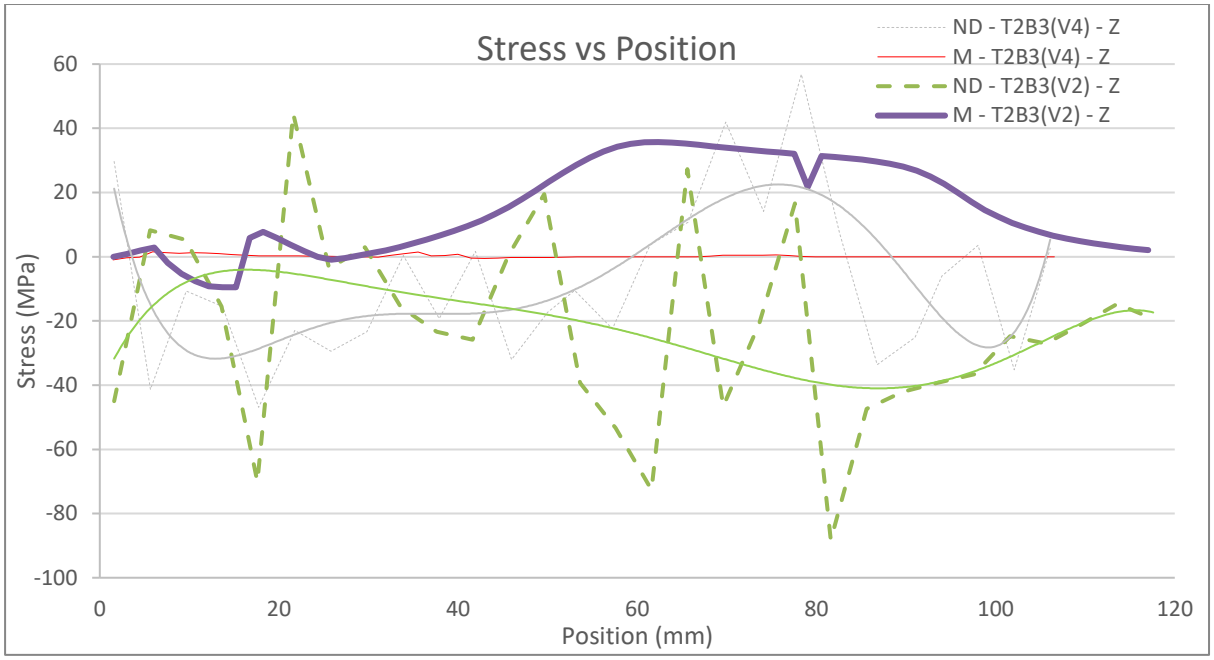

Figure 46: T2B3(V2) vs T2B3(V4) machined - MAGMASOFT® vs neutron diffraction result in the z-direction of the z-direction stress component

It cannot be assumed that the machining of components always reduces the residual stress therein. The reason for this is due to the fact that the branches measured in this study are geometrically very simple, whereas the machining of components with more complex geometries might cause an increase in residual stresses.

6.3 Summary

The results obtained were sufficient enough to be able to make a conclusion. Although major improvements could have been made to obtain more efficient results, these improvements are discussed in section 7.1.

Possible reasons for results to differ between MAGMASOFT® and neutron diffraction measurements:

- The casing was not cast 100% symmetrical (supported by section 4.1.2 and Figure 23).
- MAGMASOFT® simulated within perfect conditions.
- The measurements between MAGMASOFT® and the neutron diffraction measurements were not taken at the exact same locations/positions due to the casting offset.

- The cope and the drag of the mould was not clamped and sealed correctly causing a leak through the mould forming a large flash, which possibly influenced the residual stress results (supported by section 4.1.2, section 4.2. and Figure 28).

- The material used for casting of the trees could have differed slightly in composition with that specified in the simulation and between the different trees that were cast.

A similar study was discovered in the literature completed by Johnson *et al*. (2012:1487). The difference between the MAGMASOFT® and neutron diffraction results were found to be in the same order (up to 35 MPa in difference) as in this study. According to Johnson's summary, his results were very good. One of the residual stress measurements completed by Johnson *et al*. (2012:1495) can be viewed in Figure 47 below.

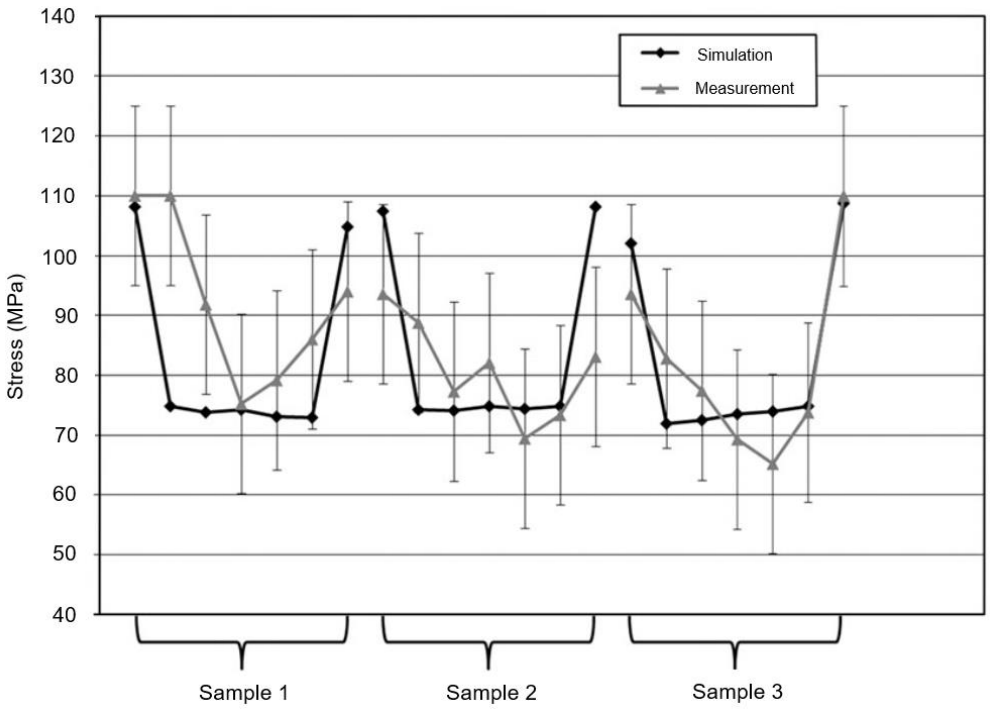

Figure 47: Residual stress results between simulated (MAGMASOFT®) and measured (neutron diffraction) completed by Johnson *et al*. (2012:1495)

7. FUTURE RESEARCH AND CONCLUSION

7.1 Future Research

Future research can be carried out by means of measuring samples that consist of much higher residual stresses which can more accurately be tested by means of neutron diffraction. The neutron diffraction statistics could also be improved by increasing the measurement time per position; for this longer beam times are required. Utmost care must also be taken that the castings are perfected and all the different samples must be cast under the same conditions.

The effect that different heat treatment processes have on the residual stress results can be verified, and more complex components can be verified for machining related residual stress.

In future research, MAGMASOFT® residual stress results can also be verified by means of other methods or even multiple methods, simultaneously.

7.2 Conclusion

The neutron diffraction measurement times per position were not sufficient to reduce the fitting error to accurately establish a stress trend through the samples. This caused that the error bars were to immense and the data could not be accurately compared to the MAGMASOFT® results. The reason for the insufficient beam time was due to the beam time allocated to this project by the personnel at Necsa SOC Limited.

The data collected suggests that MAGMASOFT® can be used to simulate the residual stress in the casting process and, more specifically, simulate residual stress in valves as it uses conservative measures. However, the accuracy thereof remains unknown at this point in time.

References

Abou Msallem, Y., Jacquemin, F., Boyard, N., Poitou, A., Delaunay, D. & Chatel, S. 2010. Material characterization and residual stresses simulation during the manufacturing process of epoxy matrix composites. *Composites Part A: Applied Science and Manufacturing*, 41(1):108-115.

Ali Fatemi-University of Toledo. Residual stresses and their effects on fatigue resistance. https://www.efatigue.com/training/Chapter_8.pdf Date of access: 29 May 2016.

Anon. 2009. Cast Iron (EN-GJS). http://www.sn-castiron.nl/en/castiron/en_gjs.html Date of access: 4 July 2017.

Anon. 2014. EN-GJS-400-15, GGG40 Cast Iron Material. http://www.iron-foundry.com/en-gjs-400-15-ggg40-cast-iron.html Date of access: 4 July 2017.

AtlasFoundry-Inc. 2016. Understanding Cast Irons - Ductile Iron. http://www.atlasfdry.com/ductile-iron.htm Date of access: 15 August 2017.

Bonnaud, E. & Gunnars, J. 2015. Three Dimensional Weld Residual Stresses Simulations of Start/Stop and Weld Repair Effects. *Procedia Engineering*, 130(2015):531-543.

Cañas, J., Picón, R., Paris, F. & Del Rio, J.I. 1996. A one-dimensional model for the prediction of residual stress and its relief in welded plates. *International Journal of Mechanical Sciences*, 38(7):735-751.

Combrinck, G. 2017. Integration of cast simulated mechanical properties into FEA for improved tensile strength evaluation of ductile iron gate valve bodies. Potchefstroom: NWU. (Dissertation - MEng).

Dura-Bar. 2016. Dura-Bar Heat-Treating Guide. http://www.dura-bar.com/resources/upload/Dura-Bar-Heat-Treating-Guide.pdf Date of access: 2 May 2017.

He, B. 2005. Computer Modeling of Weld Joint Microstructure and Residual Stresses. Ottawa, Canada: Carleton University. (Dissertation - MEng).

Hoffman, J.W. & DeBeer, F.C. 2012. Characteristics of the Micro-Focus X-ray Tomography Facility (MIXRAD) at Necsa in South Africa. Paper presented at the 18th World Conference on Non-destructive Testing, Durban, South Africa.

James, M.R. & Buck, O. 2006. Quantitative nondestructive measurements of residual stresses. *Critical Reviews in Solid State and Materials Sciences*, 9(1):61-105.

Johnson, E.M., Watkins, T.R., Schmidlin, J.E. & Dutler, S.A. 2012. A Benchmark Study on Casting Residual Stress. *Metallurgical and Materials Transactions A*, 43A(5):1487-1496.

Kalpakjian, S. & Schmid, S.R. 2014. Manufacturing Engineering and Technology. Singapore: Pearson Education.

KITZ-Corporation. 2008. Valve Materials. https://www.kitz.co.jp/english2/material_index.html Date of access: 26 May 2016.

MAGMA. 2012a. MAGMA - Company Pofile. http://www.magmasoft.com/en/company/company-profile.html Date of access: 1 June 2016.

MAGMA. 2012b. MAGMA - fully optimize. http://www.magmasoft.com/en/solutions/MAGMA_5.html Date of access: 31 May 2016.

MAGMA. 2012c. MAGMA Solutions. http://www.magmasoft.com/en/solutions/MAGMA_5.html Date of access: 31 May 2016.

MAGMA. 2017. MAGMASOFT - Autonomous engineering. https://www.magmasoft.de/en/solutions/magmasoft/ Date of access: 15 August 2017.

Makino, A. 1994. Measurement of residual stresses using the holographic hole drilling technique. California: Stanford University. (Thesis - PhD).

Marais, D. 2016. Operational optimization of the Necsa SAFARI-1 neutron diffraction strain scanner. Potchefstroom: NWU. (Thesis - PhD).

Marais, D. & Venter, A. 2017. MPISI - Materials Probe for Internal Strain Investigations. http://www.necsa.co.za/Products-and-Services/Research/Facility-and-Instrument-characteristics/MPISI Date of access: 29 August 2017.

Marais, D., Venter, A.M. & Markgraaff, J. 2016. Optimisation of counting time using count statistics on a diffraction beamline. *Nuclear Instruments and Methods in Physics Research A*, 818(2016):32-37.

McFarlane, A. 2016. Valve Casting in South Africa [personal interview]. Aug., Ametex (Pty) Ltd., Boksburg, South Africa.

Merchantec-research. Industry, T.A. 2014. Industry Supply Analysis: Deliverable 1.

Nye, J.F. 1985. Physical properties of crystals - their representation by tensors and matrices. USA: Oxford.

Paradowska, A., Price, J.W.H., Ibrahim, R. & Finlayson, T. 2005. A neutron diffraction study of residual stress due to welding. *Journal of Materials Processing Technology*, 164-165(2005):1099-1105.

Parry, L., Ashcroft, I.A. & Wildman, R.D. 2016. Understanding the effect of laser scan strategy on residual stress in selective laser melting through thermo-mechanical simulation. *Additive Manufacturing*.

Pintschovius, L., Jung, V., Macherauch, E. & Vohringer, O. 1983. Residual Stress Measurements by means of Neutron Diffraction. *Materials Science and Engineering*, 61(1983):43-50.

Ramakrishnan, K. 1998. Evaluation of Residual Stress in Cast Iron by an Ultrasonic Technique. Texas:Lamar University. (Dissertation - MEng).

Shekhar, S. & Jaiswal, A. 2008. Heat treatment of S.G. cast iron and its effects. National Institute of Technology Rourkela.

Solken, W. 2008. Explore the world of piping. http://www.wermac.org/valves/valves_general.html Date of access: 26 May 2016.

Warda, R.D. 1990. Ductile Iron Data for Design Engineers: QIT-Fer et Titane Inc.

Webster, G.A. & Ezeilo, A.N. 1997. Neutron scattering in engineering applications. *Physica B: Condensed Matter*, 234-236(1997):949-955.

Webster, G.A. & Wimpory, R.C. 2001. Non-destructive measurement of residual stress by neutron diffraction. *Journal of Materials Processing Technology*, 117:395-399.

Yaghi, A., Hyde, T.H., Becker, A.A., Sun, W. & Williams, J.A. 2006. Residual stress simulation in thin and thick-walled stainless steel pipe welds including pipe diameter effects. *International Journal of Pressure Vessels and Piping*, 83(11-12):864-874.

Zhang, W., Fang, K., Hu, Y., Wang, S. & Wang, X. 2016. Effect of machining-induced surface residual stress on initiation of stress corrosion cracking in 316 austenitic stainless steel. *Corrosion Science*, 108:173-184.

Appendix A

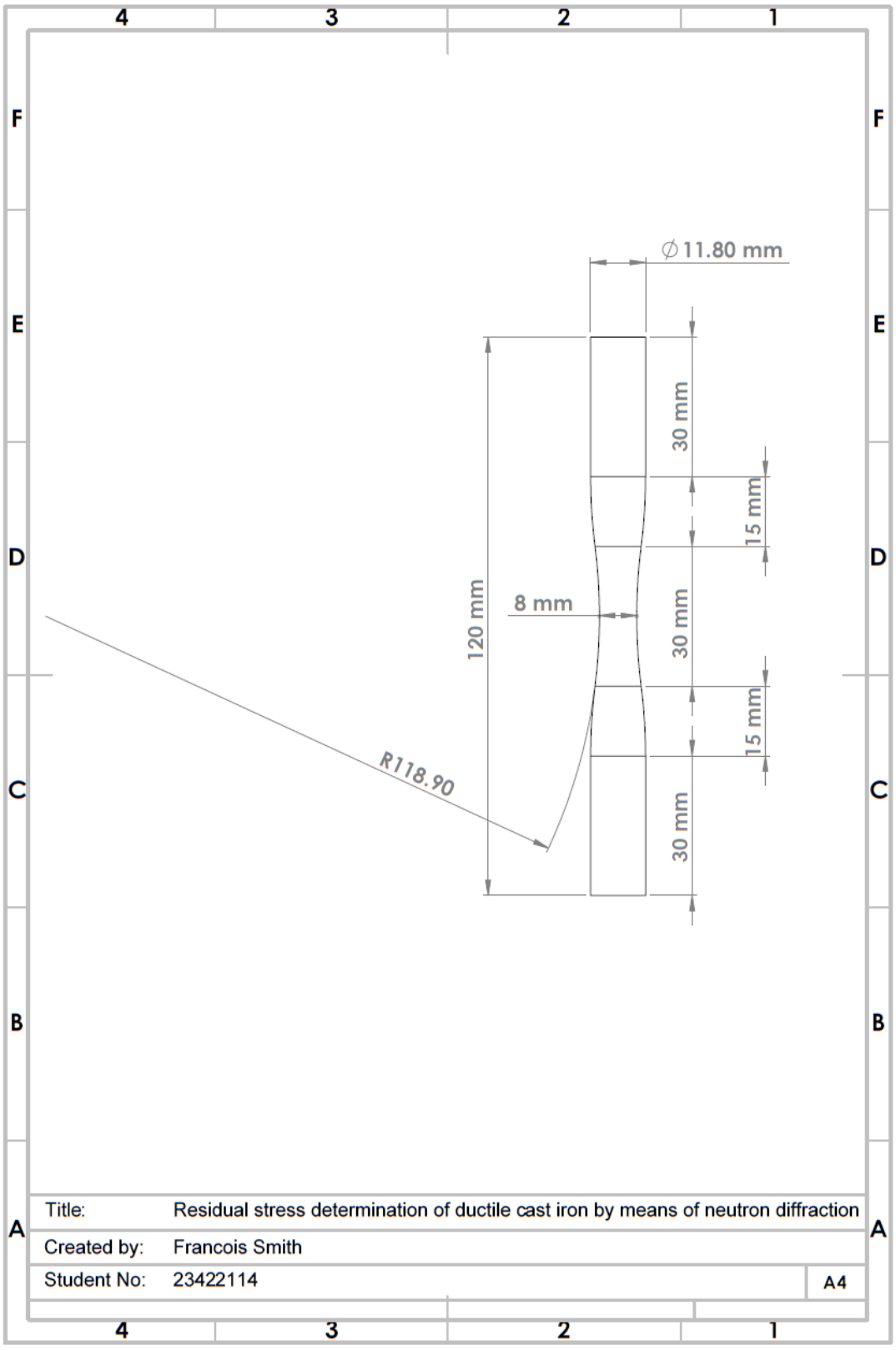

Figure 48: Detail drawing and measurements of the machined samples - T2B1(V4), T2B2(V4) and T2B3(V4)

Appendix B

B.1 T1B1(V2) residual stress results

T1B1(V2) x-component residual stresses in z-direction				T1B1(V2) y-component residual stresses in z-direction				T1B1(V2) z-component residual stresses in z-direction			
Neutron Diffraction		MAGMASOFT		Neutron Diffraction		MAGMASOFT		Neutron Diffraction		MAGMASOFT	
Stress	Position	Stress	Position	Stress	Position	Stress	Position	Stress	Position	Stress	Position
-10.55	1.60	-0.52	1.52	75.84	1.60	0.12	1.52	-1.78	1.60	1.99	1.52
43.86	5.60	0.19	3.04	28.21	5.60	0.90	3.04	3.59	5.60	1.38	3.04
21.38	9.60	1.05	4.56	27.75	9.60	2.74	4.56	27.26	9.60	-1.00	4.56
6.02	13.60	-7.40	6.08	17.21	13.60	6.94	6.08	9.22	13.60	2.25	6.08
7.01	17.60	1.64	7.60	11.97	17.60	1.37	7.60	-23.61	17.60	-3.20	7.60
42.26	21.60	5.20	9.12	35.57	21.60	-22.00	9.12	28.86	21.60	-1.68	9.12
-12.88	25.60	-4.81	10.64	-11.38	25.60	0.60	10.64	-73.05	25.60	11.80	10.64
31.62	29.60	-3.36	12.16	30.42	29.60	0.16	12.16	65.79	29.60	12.45	12.16
-57.48	33.60	-2.42	13.68	-51.15	33.60	-0.04	13.68	-92.57	33.60	12.76	13.68
-34.28	37.60	-2.07	15.20	-10.79	37.60	-0.12	15.20	-45.57	37.60	12.94	15.20
55.41	41.60	-1.81	16.72	66.57	41.60	-0.15	16.72	18.95	41.60	12.94	16.72
-24.91	45.60	-1.63	18.24	20.58	45.60	-0.16	18.24	-1.32	45.60	12.86	18.24
-1.49	49.60	-1.38	19.76	-6.97	49.60	-0.15	19.76	-24.66	49.60	12.79	19.76
-15.21	53.60	-1.07	21.28	11.94	53.60	-0.12	21.28	-28.70	53.60	12.77	21.28
29.34	57.60	-0.67	22.80	23.37	57.60	-0.05	22.80	-12.23	57.60	12.89	22.80
0.87	61.60	-0.22	24.32	39.85	61.60	0.04	24.32	13.59	61.60	13.24	24.32
-1.01	65.60	0.27	25.84	21.33	65.60	0.17	25.84	8.14	65.60	14.04	25.84
-49.20	69.60	0.65	27.36	-10.79	69.60	0.29	27.36	-99.49	69.60	15.58	27.36
-43.36	73.60	0.73	28.88	-53.80	73.60	0.37	28.88	-126.83	73.60	18.16	28.88
-82.00	77.60	0.53	30.40	-10.50	77.60	0.43	30.40	-111.99	77.60	21.39	30.40
56.63	81.60	0.42	31.92	83.38	81.60	0.48	31.92	-18.13	81.60	24.15	31.92
14.73	85.60	0.58	33.44	67.36	85.60	0.52	33.44	32.69	85.60	28.62	33.44
107.80	89.60	1.13	34.96	101.00	89.60	0.52	34.96	93.31	89.60	32.26	34.96
-2.57	93.60	2.07	36.48	-16.64	93.60	0.49	36.48	-90.14	93.60	35.75	36.48
-51.07	97.60	3.32	38.00	-27.51	97.60	0.40	38.00	-92.04	97.60	38.94	38.00
9.09	101.60	4.58	39.52	19.91	101.60	0.26	39.52	-56.00	101.60	41.67	39.52
-12.52	105.60	5.46	41.04	26.00	105.60	0.08	41.04	-28.00	105.60	43.69	41.04
-5.61	109.60	5.65	42.56	14.00	109.60	-0.11	42.56	-5.00	109.60	44.82	42.56
6.36	113.60	4.96	44.08	9.00	113.60	-0.28	44.08	9.00	113.60	44.90	44.08
8.43	117.60	3.40	45.60	2.02	117.60	-0.42	45.60	25.00	117.60	43.93	45.60
		1.41	47.12			-0.47	47.12			44.90	47.12
		-0.30	48.64			-0.42	48.64			42.35	48.64
		-1.30	50.16			-0.35	50.16			39.34	50.16
		-1.72	51.68			-0.32	51.68			38.26	51.68
		-1.84	53.20			-0.33	53.20			37.27	53.20
		-1.71	54.72			-0.35	54.72			36.31	54.72
		-1.39	56.24			-0.37	56.24			35.39	56.24
		-0.93	57.76			-0.39	57.76			34.48	57.76
		-0.41	59.28			-0.41	59.28			33.56	59.28
		0.14	60.80			-0.43	60.80			32.55	60.80
		0.63	62.32			-0.44	62.32			31.45	62.32
		0.99	63.84			-0.45	63.84			30.23	63.84
		1.21	65.36			-0.48	65.36			28.92	65.36
		1.24	66.88			-0.52	66.88			27.50	66.88
		1.13	68.40			-0.60	68.40			25.99	68.40
		0.72	69.92			-0.83	69.92			24.13	69.92
		-0.48	71.44			-1.60	71.44			21.42	71.44

		-3.49	72.96			-3.60	72.96			19.35	72.96
		-5.00	74.48			-5.75	74.48			19.37	74.48
		NaN	76.00			NaN	76.00			NaN	76.00
		NaN	77.52			NaN	77.52			NaN	77.52
		NaN	79.04			NaN	79.04			NaN	79.04
		NaN	80.56			NaN	80.56			NaN	80.56
		5.38	82.08			6.59	82.08			24.13	82.08
		2.33	83.60			4.58	83.60			26.56	83.60
		4.16	85.12			3.08	85.12			29.04	85.12
		-1.39	86.64			1.52	86.64			33.58	86.64
		-1.48	88.16			1.00	88.16			36.72	88.16
		-1.12	89.68			0.81	89.68			39.07	89.68
		-0.59	91.20			0.72	91.20			41.08	91.20
		-0.01	92.72			0.65	92.72			42.96	92.72
		0.56	94.24			0.58	94.24			44.86	94.24
		1.40	95.76			0.50	95.76			46.84	95.76
		1.37	97.28			0.40	97.28			48.90	97.28
		1.46	98.80			0.28	98.80			51.00	98.80
		1.25	100.32			0.18	100.32			53.13	100.32
		0.45	101.84			0.15	101.84			55.31	101.84
		-1.05	103.36			0.16	103.36			57.55	103.36
		-2.93	104.88			0.15	104.88			59.44	104.88
		-4.41	106.40			0.07	106.40			60.58	106.40
		-4.99	107.92			-0.03	107.92			60.47	107.92
		-4.98	109.44			-0.15	109.44			59.38	109.44
		-4.24	110.96			-0.29	110.96			57.27	110.96
		-3.08	112.48			-0.43	112.48			54.49	112.48
		-1.73	114.00			-0.54	114.00			51.07	114.00
		-0.47	115.52			-0.67	115.52			47.27	115.52
		0.42	117.04			-0.76	117.04			43.10	117.04

B.2 T1B2(V2) and T1B3(V2) residual stress results

T1B2(V2) z-component residual stresses in z-direction				T1B3(V2) z-component residual stresses in z-direction				T1B3(V2) z-component residual stresses in x-direction			
Neutron Diffraction		MAGMASOFT		Neutron Diffraction		MAGMASOFT		Neutron Diffraction		MAGMASOFT	
Stress	Position	Stress	Position	Stress	Position	Stress	Position	Stress	Position	Stress	Position
1.60	35.35	14.56	1.52	-50.90	1.60	0.01	1.52	-37.00	-11.06	0.27	-11.06
5.60	-3.16	16.11	3.04	2.11	5.60	0.87	3.04	-40.82	-9.21	0.24	-10.82
9.60	-20.75	17.80	4.56	18.27	9.60	1.95	4.56	-45.81	-7.37	0.24	-10.58
13.60	4.47	18.61	6.08	-62.28	13.60	2.81	6.08	-54.81	-5.53	0.24	-10.33
17.60	-4.61	6.26	7.60	-116.03	17.60	-1.97	7.60	1.48	-3.69	0.29	-10.09
21.60	-18.55	1.45	9.12	-2.09	21.60	-5.35	9.12	-17.35	-1.84	0.42	-9.85
25.60	-7.12	0.56	10.64	59.80	25.60	-7.66	10.64	14.80	0.00	0.55	-9.61
29.60	-12.27	-0.08	12.16	-49.64	29.60	-9.16	12.16	48.02	1.84	0.68	-9.37
33.60	-14.85	-4.71	13.68	-1.77	33.60	-9.51	13.68	13.96	3.69	0.81	-9.12
37.60	-12.43	1.36	15.20	-32.00	37.60	-9.52	15.20	21.64	5.53	0.94	-8.88
41.60	-9.86	-0.45	16.72	-21.90	41.60	5.82	16.72	-19.71	7.37	1.07	-8.64
45.60	2.07	-2.18	18.24	135.11	45.60	7.74	18.24	35.51	9.22	1.20	-8.40
49.60	-30.57	-1.35	19.76	-40.13	49.60	5.87	19.76	36.22	11.06	1.39	-8.16
53.60	-14.43	-1.19	21.28	-99.14	53.60	3.80	21.28	47.01	12.90	1.58	-7.91
57.60	-20.99	-0.22	22.80	-97.16	57.60	1.76	22.80			1.77	-7.67
61.60	-8.66	0.17	24.32	69.35	61.60	-0.01	24.32			1.96	-7.43
65.60	-12.89	-0.08	25.84	-160.72	65.60	-0.91	25.84			2.15	-7.19
69.60	8.96	0.27	27.36	-65.21	69.60	-0.47	27.36			2.33	-6.95
73.60	3.60	-0.07	28.88	11.45	73.60	0.41	28.88			2.52	-6.70
77.60	4.75	-0.06	30.40	90.30	77.60	1.18	30.40			2.53	-6.46
81.60	-30.13	-0.05	31.92	-29.74	81.60	2.00	31.92			2.52	-6.22
85.60	-4.78	-0.08	33.44	51.13	85.60	2.97	33.44			2.51	-5.98
89.60	10.37	-0.07	34.96	29.00	89.60	4.12	34.96			2.50	-5.74
93.60	11.77	0.08	36.48	45.41	93.60	5.35	36.48			2.48	-5.49
97.60	4.25	-0.03	38.00	-107.54	97.60	6.64	38.00			2.47	-5.25
101.60	-6.45	0.17	39.52	-65.05	101.60	8.00	39.52			2.46	-5.01
105.60	11.24	0.11	41.04	54.86	105.60	9.51	41.04			1.98	-4.77
109.60	14.84	-0.20	42.56	69.46	109.60	11.21	42.56			1.27	-4.53
113.60	18.72	-0.20	44.08	-103.04	113.60	13.18	44.08			0.56	-4.28
117.60	3.23	3.25	45.60	51.32	117.60	15.38	45.60			-0.16	-4.04
		6.52	47.12			17.89	47.12			-0.87	-3.80
		9.71	48.64			20.61	48.64			-1.54	-3.56
		5.00	50.16			23.37	50.16			-1.94	-3.32
		5.59	51.68			26.07	51.68			-2.36	-3.07
		5.03	53.20			28.59	53.20			-2.77	-2.83
		3.23	54.72			30.88	54.72			-3.11	-2.59
		2.27	56.24			32.81	56.24			-3.30	-2.35
		3.21	57.76			34.30	57.76			-3.48	-2.11
		4.99	59.28			35.20	59.28			-3.67	-1.86
		8.41	60.80			35.64	60.80			-3.81	-1.62
		12.17	62.32			35.71	62.32			-3.89	-1.38
		15.64	63.84			35.53	63.84			-3.97	-1.14
		18.50	65.36			35.21	65.36			-4.05	-0.90
		20.03	66.88			34.82	66.88			-4.09	-0.65
		19.80	68.40			34.39	68.40			-4.11	-0.41
		19.45	69.92			33.96	69.92			-4.13	-0.17
		19.69	71.44			33.55	71.44			-4.15	0.07
		20.08	72.96			33.16	72.96			-4.13	0.31
		20.45	74.48			32.79	74.48			-4.10	0.56
		20.79	76.00			32.43	76.00			-4.07	0.80

		21.17	77.52			32.08	77.52			-4.04	1.04
		21.52	79.04			21.74	79.04			-3.97	1.28
		21.80	80.56			31.40	80.56			-3.89	1.53
		22.03	82.08			31.06	82.08			-3.82	1.77
		22.28	83.60			30.68	83.60			-3.75	2.01
		22.64	85.12			30.25	85.12			-3.64	2.25
		23.16	86.64			29.72	86.64			-3.54	2.49
		23.90	88.16			29.02	88.16			-3.44	2.74
		24.68	89.68			28.09	89.68			-3.33	2.98
		25.33	91.20			26.77	91.20			-3.22	3.22
		25.96	92.72			25.03	92.72			-3.10	3.46
		26.91	94.24			22.70	94.24			-2.99	3.70
		28.55	95.76			19.99	95.76			-2.89	3.95
		31.48	97.28			17.14	97.28			-2.81	4.19
		35.43	98.80			14.56	98.80			-2.72	4.43
		40.42	100.32			12.40	100.32			-2.64	4.67
		44.86	101.84			10.56	101.84			-2.75	4.91
		41.49	103.36			9.02	103.36			-2.95	5.16
		29.03	104.88			7.69	104.88			-3.01	5.40
		18.02	106.40			6.57	106.40			-3.37	5.64
		10.64	107.92			5.61	107.92			-2.14	5.88
		5.13	109.44			4.81	109.44			-0.59	6.12
		1.45	110.96			4.13	110.96			0.96	6.37
		0.14	112.48			3.53	112.48			2.51	6.61
		0.01	114.00			2.98	114.00			4.06	6.85
		0.01	115.52			2.48	115.52			5.04	7.09
		0.22	117.04			2.03	117.04			4.89	7.33
										4.74	7.58
										4.59	7.82
										4.43	8.06
										4.28	8.30
										4.13	8.54
										3.97	8.79
										3.75	9.03
										3.54	9.27
										3.32	9.51
										3.11	9.75
										2.89	10.00
										2.67	10.24
										2.46	10.48
										2.22	10.72
										1.99	10.96
										1.76	11.21
										1.52	11.45
										1.29	11.69
										1.05	11.93
										0.82	12.17
										0.80	12.42
										0.80	12.66
										0.80	12.90

B.3 T2B3(V2) residual stress results

T2B3(V2) z-component residual stresses in z-direction			
Neutron Diffraction		MAGMASOFT	
Stress	Position	Stress	Position
-24.40	1.60	0.01	1.52
28.83	5.60	0.87	3.04
25.80	9.60	1.95	4.56
5.11	13.60	2.81	6.08
-49.57	17.60	-1.97	7.60
65.16	21.60	-5.35	9.12
16.94	25.60	-7.66	10.64
23.51	29.60	-9.16	12.16
4.88	33.60	-9.51	13.68
-2.80	37.60	-9.52	15.20
-5.27	41.60	5.82	16.72
20.93	45.60	7.74	18.24
40.12	49.60	5.87	19.76
-18.75	53.60	3.80	21.28
-32.77	57.60	1.76	22.80
-52.03	61.60	-0.01	24.32
47.89	65.60	-0.91	25.84
-26.03	69.60	-0.47	27.36
-0.37	73.60	0.41	28.88
37.24	77.60	1.18	30.40
-67.70	81.60	2.00	31.92
-26.81	85.60	2.97	33.44
-21.56	89.60	4.12	34.96
-18.63	93.60	5.35	36.48
-16.02	97.60	6.64	38.00
-4.20	101.60	8.00	39.52
-6.43	105.60	9.51	41.04
-0.50	109.60	11.21	42.56
5.91	113.60	13.18	44.08
1.22	117.60	15.38	45.60
		17.89	47.12
		20.61	48.64
		23.37	50.16
		26.07	51.68
		28.59	53.20
		30.88	54.72
		32.81	56.24
		34.30	57.76
		35.20	59.28
		35.64	60.80
		35.71	62.32
		35.53	63.84
		35.21	65.36
		34.82	66.88
		34.39	68.40
		33.96	69.92
		33.55	71.44
		33.16	72.96
		32.79	74.48
		32.43	76.00
		32.08	77.52
		21.74	79.04
		31.40	80.56
		31.06	82.08
		30.68	83.60
		30.25	85.12
		29.72	86.64
		29.02	88.16
		28.09	89.68

		26.77	91.20
		25.03	92.72
		22.70	94.24
		19.99	95.76
		17.14	97.28
		14.56	98.80
		12.40	100.32
		10.56	101.84
		9.02	103.36
		7.69	104.88
		6.57	106.40
		5.61	107.92
		4.81	109.44
		4.13	110.96
		3.53	112.48
		2.98	114.00
		2.48	115.52
		2.03	117.04

B.4 T1B1(V3), T1B1(V3) and T1B1(V3) residual stress results

T1B1(V3) z-component residual stresses in z-direction				T1B2(V3) z-component residual stresses in z-direction				T1B3(V3) z-component residual stresses in z-direction			
Neutron Diffraction		MAGMASOFT		Neutron Diffraction		MAGMASOFT		Neutron Diffraction		MAGMASOFT	
Stress	Position	Stress	Position	Stress	Position	Stress	Position	Stress	Position	Stress	Position
43.73	1.60	1.73	1.52	15.83	1.60	10.16	1.52	-18.10	1.60	0.54	1.52
48.27	5.60	1.20	3.04	8.83	5.60	10.37	3.04	6.66	5.60	1.10	3.04
9.28	9.60	-1.40	4.56	10.96	9.60	11.22	4.56	-13.70	9.60	1.94	4.56
18.82	13.60	-2.89	6.08	-35.15	13.60	13.02	6.08	40.63	13.60	2.86	6.08
48.70	17.60	-5.52	7.60	17.79	17.60	7.24	7.60	-3.75	17.60	-1.51	7.60
46.58	21.60	-1.63	9.12	-13.11	21.60	3.22	9.12	-37.67	21.60	-4.58	9.12
-44.26	25.60	10.63	10.64	-7.55	25.60	0.77	10.64	28.37	25.60	-6.63	10.64
-19.76	29.60	11.13	12.16	18.23	29.60	-0.18	12.16	30.78	29.60	-7.93	12.16
-16.90	33.60	11.30	13.68	-10.16	33.60	0.68	13.68	-19.37	33.60	-8.22	13.68
-31.94	37.60	11.30	15.20	-10.41	37.60	0.00	15.20	-23.61	37.60	-8.36	15.20
-20.07	41.60	11.12	16.72	0.95	41.60	-1.01	16.72	44.61	41.60	5.21	16.72
28.07	45.60	10.86	18.24	12.92	45.60	-1.98	18.24	-39.18	45.60	7.02	18.24
-25.90	49.60	10.58	19.76	-25.65	49.60	-1.24	19.76	-5.44	49.60	5.46	19.76
-53.33	53.60	10.33	21.28	-26.39	53.60	-1.09	21.28	-6.42	53.60	3.65	21.28
-32.76	57.60	10.17	22.80	3.29	57.60	-0.18	22.80	-7.54	57.60	1.78	22.80
-15.43	61.60	10.19	24.32	10.69	61.60	0.22	24.32	14.87	61.60	0.09	24.32
-1.99	65.60	10.59	25.84	23.71	65.60	0.23	25.84	-12.05	65.60	-0.92	25.84
18.43	69.60	11.59	27.36	-4.65	69.60	0.23	27.36	-0.85	69.60	-0.54	27.36
-46.10	73.60	13.37	28.88	-9.48	73.60	-0.05	28.88	-6.09	73.60	0.29	28.88
8.70	77.60	15.55	30.40	14.38	77.60	-0.06	30.40	3.23	77.60	0.90	30.40
26.84	81.60	17.88	31.92	-11.89	81.60	-0.05	31.92	14.02	81.60	1.46	31.92
-26.41	85.60	20.21	33.44	4.91	85.60	-0.08	33.44	-12.43	85.60	2.14	33.44
18.59	89.60	22.48	34.96	7.88	89.60	-0.06	34.96	3.36	89.60	2.95	34.96
-19.91	93.60	24.62	36.48	-14.96	93.60	0.08	36.48	6.43	93.60	3.85	36.48
-28.74	97.60	26.54	38.00	4.23	97.60	-0.02	38.00	2.43	97.60	4.79	38.00
20.40	101.60	28.17	39.52	4.40	101.60	0.16	39.52	-52.80	101.60	5.81	39.52
7.41	105.60	29.38	41.04	16.42	105.60	0.10	41.04	-41.40	105.60	6.98	41.04
-13.28	109.60	30.09	42.56	39.67	109.60	-0.16	42.56	-17.82	109.60	8.31	42.56
-77.56	113.60	30.23	44.08	-8.80	113.60	-0.23	44.08	5.88	113.60	9.78	44.08
-26.69	117.60	29.77	45.60	-9.72	117.60	3.16	45.60	-35.67	117.60	11.29	45.60
		28.89	47.12			6.20	47.12			12.81	47.12
		27.89	48.64			9.16	48.64			14.27	48.64
		27.01	50.16			-0.43	50.16			15.56	50.16
		26.26	51.68			5.53	51.68			16.72	51.68
		25.57	53.20			4.78	53.20			17.75	53.20
		24.93	54.72			3.02	54.72			18.65	54.72
		24.36	56.24			1.87	56.24			19.38	56.24
		23.89	57.76			2.74	57.76			19.89	57.76
		23.47	59.28			4.17	59.28			20.13	59.28
		23.06	60.80			6.82	60.80			20.16	60.80
		22.63	62.32			9.49	62.32			20.00	62.32
		22.12	63.84			11.60	63.84			19.75	63.84
		21.53	65.36			13.06	65.36			19.44	65.36
		20.80	66.88			13.67	66.88			19.11	66.88
		19.92	68.40			13.57	68.40			18.80	68.40
		18.69	69.92			13.47	69.92			18.53	69.92
		16.70	71.44			13.60	71.44			18.29	71.44
		14.88	72.96			13.80	72.96			18.10	72.96
		14.64	74.48			13.99	74.48			17.94	74.48
		NaN	76.00			14.15	76.00			17.82	76.00
		NaN	77.52			14.29	77.52			17.74	77.52

		NaN	79.04			14.38	79.04			17.68	79.04
		NaN	80.56			14.44	80.56			17.66	80.56
		17.41	82.08			14.48	82.08			17.66	82.08
		19.25	83.60			14.54	83.60			17.68	83.60
		20.71	85.12			14.64	85.12			17.70	85.12
		23.46	86.64			14.81	86.64			17.70	86.64
		25.00	88.16			15.06	88.16			17.64	88.16
		25.98	89.68			15.31	89.68			17.47	89.68
		26.77	91.20			15.50	91.20			17.11	91.20
		27.52	92.72			15.70	92.72			16.50	92.72
		28.31	94.24			16.13	94.24			15.53	94.24
		29.21	95.76			16.96	95.76			14.23	95.76
		30.18	97.28			18.40	97.28			12.67	97.28
		31.20	98.80			20.22	98.80			11.08	98.80
		32.24	100.32			22.10	100.32			9.58	100.32
		33.32	101.84			23.22	101.84			8.22	101.84
		34.49	103.36			21.20	103.36			7.03	103.36
		35.57	104.88			15.29	104.88			5.99	104.88
		36.29	106.40			9.65	106.40			5.10	106.40
		36.42	107.92			5.50	107.92			4.35	107.92
		36.08	109.44			0.98	109.44			3.37	109.44
		35.20	110.96			0.44	110.96			3.22	110.96
		33.90	112.48			0.09	112.48			2.78	112.48
		32.18	114.00			0.00	114.00			2.38	114.00
		30.17	115.52			0.05	115.52			2.00	115.52
		27.87	117.04			0.34	117.04			1.66	117.04

B.5 T2B1(V4), T2B1(V4) and T2B1(V4) residual stress results

T2B1(V4) z-component residual stresses in z-direction				T2B2(V4) z-component residual stresses in z-direction				T2B3(V4) z-component residual stresses in z-direction			
Neutron Diffraction		MAGMASOFT		Neutron Diffraction		MAGMASOFT		Neutron Diffraction		MAGMASOFT	
Stress	Position	Stress	Position	Stress	Position	Stress	Position	Stress	Position	Stress	Position
17.00	1.60	0.10	1.48	3.00	1.60	-0.05	1.48	29.69	1.60	-0.98	1.48
7.08	5.63	-0.05	2.96	4.76	5.64	0.23	2.96	-41.27	5.64	-0.36	2.96
-34.01	9.67	-0.78	4.44	37.95	9.67	0.59	4.44	-10.69	9.67	-0.10	4.44
20.27	13.70	0.06	5.92	-17.77	13.70	-0.75	5.92	-15.46	13.70	1.53	5.92
-49.26	17.73	0.14	7.40	-29.98	17.73	-0.56	7.40	-46.91	17.73	1.22	7.40
-24.57	21.77	0.24	8.88	-16.29	21.77	0.13	8.88	-23.01	21.77	1.09	8.88
-21.99	25.80	0.53	10.36	-16.46	25.80	0.14	10.36	-29.47	25.80	1.24	10.36
-37.18	29.83	0.20	11.84	33.12	29.83	0.32	11.84	-23.41	29.83	1.19	11.84
-9.10	33.87	-0.04	13.32	-66.14	33.87	-0.05	13.32	0.40	33.87	0.96	13.32
-45.28	37.90	-0.03	14.80	41.62	37.90	-0.03	14.80	-19.23	37.90	0.66	14.80
-5.58	41.93	0.73	16.28	-10.26	41.93	-0.01	16.28	1.67	41.93	0.44	16.28
7.90	45.97	2.24	17.76	-33.05	45.97	-0.04	17.76	-32.07	45.97	0.31	17.76
10.50	50.00	3.98	19.24	-27.17	50.00	0.00	19.24	-17.31	50.00	0.28	19.24
22.37	53.00	5.80	20.72	-75.00	53.00	0.32	20.72	-10.54	53.00	0.26	20.72
-4.50	57.22	7.61	22.20	-2.10	57.22	-0.08	22.20	-22.50	57.22	0.24	22.20
39.53	61.44	9.36	23.68	-69.93	61.45	0.19	23.68	3.72	61.45	0.20	23.68
85.59	65.67	10.98	25.16	-66.52	65.67	0.14	25.16	10.69	65.67	0.14	25.16
-25.89	69.89	12.36	26.64	-41.81	69.89	-0.27	26.64	41.88	69.89	0.07	26.64
-0.94	74.11	13.30	28.12	-43.66	74.11	1.30	28.12	14.09	74.11	0.03	28.12
-2.08	78.34	13.62	29.60	-70.30	78.33	4.48	29.60	56.83	78.33	-0.01	29.60
46.56	82.56	13.14	31.08	0.47	82.56	6.86	31.08	7.50	82.56	-0.14	31.08
13.11	86.78	11.89	32.56	-6.08	86.78	9.69	32.56	-33.61	86.78	0.42	32.56
-37.51	91.00	10.25	34.04	-27.96	91.00	7.30	34.04	-25.12	91.00	1.01	34.04
-29.46	94.00	8.64	35.52	-60.23	94.00	3.15	35.52	-6.02	94.00	1.42	35.52
-36.87	98.03	7.39	37.00	-12.15	98.03	2.84	37.00	3.53	98.03	0.25	37.00
-39.92	102.07	6.47	38.48	-2.82	102.07	2.00	38.48	-35.21	102.07	0.39	38.48
48.66	106.10	5.85	39.96	-5.75	106.10	0.79	39.96	2.70	106.10	0.77	39.96
		5.46	41.44			0.81	41.44			-0.41	41.44
		5.09	42.92			1.49	42.92			-0.53	42.92
		4.65	44.40			3.97	44.40			-0.45	44.40
		4.19	45.88			6.69	45.88			-0.25	45.88
		3.70	47.36			8.93	47.36			-0.23	47.36
		3.14	48.84			10.28	48.84			-0.24	48.84
		2.49	50.32			10.24	50.32			-0.26	50.32
		1.86	51.80			8.73	51.80			-0.12	51.80
		1.34	53.28			7.45	53.28			-0.01	53.28
		0.92	54.76			6.84	54.76			0.00	54.76
		0.56	56.24			6.59	56.24			0.00	56.24
		0.24	57.72			6.49	57.72			0.00	57.72
		0.03	59.20			6.41	59.20			0.01	59.20
		-0.57	60.68			6.41	60.68			0.01	60.68
		NaN	62.16			6.45	62.16			0.01	62.16
		NaN	63.64			6.56	63.64			0.01	63.64
		NaN	65.12			6.77	65.12			0.00	65.12
		NaN	66.60			7.07	66.60			0.01	66.60
		2.02	68.08			7.73	68.08			0.19	68.08
		2.24	69.56			8.91	69.56			0.48	69.56
		2.87	71.04			10.33	71.04			0.46	71.04
		4.07	72.52			11.50	72.52			0.43	72.52
		5.14	74.00			12.30	74.00			0.44	74.00
		5.96	75.48			13.19	75.48			0.57	75.48
		6.67	76.96			14.61	76.96			0.41	76.96

		7.43	78.44			17.18	78.44			0.10	78.44
		8.27	79.92			21.01	79.92			-0.05	79.92
		9.07	81.40			25.51	81.40			0.00	81.40
		9.85	82.88			31.40	82.88			-0.01	82.88
		10.84	84.36			37.37	84.36			-0.04	84.36
		12.07	85.84			35.82	85.84			-0.05	85.84
		13.52	87.32			25.06	87.32			-0.06	87.32
		15.10	88.80			15.48	88.80			-0.06	88.80
		16.57	90.28			9.25	90.28			-0.06	90.28
		17.60	91.76			4.48	91.76			-0.06	91.76
		17.82	93.24			1.06	93.24			-0.06	93.24
		17.43	94.72			0.08	94.72			-0.06	94.72
		16.42	96.20			0.02	96.20			-0.05	96.20
		15.03	97.68			0.09	97.68			-0.04	97.68
		13.32	99.16			0.09	99.16			-0.03	99.16
		11.43	100.64			0.41	100.64			-0.02	100.64
		9.40	102.12			0.73	102.12			-0.02	102.12
		7.26	103.60			0.79	103.60			-0.01	103.60
		5.08	105.08			0.49	105.08			-0.01	105.08
		3.06	106.56			0.74	106.56			-0.01	106.56